http://dx.doi.org/10.1016/j.apenergy.2023.121305

Multi-objective Optimization of a CO_2/H_2O Capture-based Ventilation and Air Conditioning System

Yongting Shen* and Hongxing Yang
Renewable Energy Research Group (RERG), Department of Building Environment and Energy Engineering, The Hong Kong Polytechnic University, Hong Kong, China
*Corresponding author email: yongting.shen@connect.polyu.hk

Abstract

Developing energy-efficient ventilation and air-conditioning (VAC) strategies is pivotal for achieving green buildings' triple merits of high indoor air quality (IAQ), low CO_2 emission, and low energy consumption. While adsorption-based carbon capture technologies show promising potential in improving IAQ and reducing AC energy consumption by directly removing excess CO_2/H_2O and recirculating post-captured air in buildings, current studies lack in-depth investigation into simultaneously maximizing CO_2 removal capacity and minimizing AC energy consumption. This trade-off, hindering the broad application of this technology, is rendered by the intricate interplay between indoor conditions, system configuration, and more importantly, the adsorbent materials. To circumvent this trade-off, this study proposes an NSGA-II-based multi-objective optimization model on a solar-driven CO_2/H_2O capture-based VAC system for optimizing its techno-energetic performances. This analysis maps the green buildings' merits into five constrained objectives and fully optimizes them by considering a wide spectrum of decision parameters. This analysis automatically optimized the trade-off between conflicting objectives for both studied adsorbents to various extents. While maintaining the same IAQ level, a 74% and 59% improvement in maximal captured CO_2 mass can be achieved for Mg-MOF-74 and Zeolite13X. Compared with Mg-MOF-74, Zeolites 13X performed 55% worse in maximal CO_2 removal, but 82% better in maximal energy-saving potential due to higher cyclability, stability, and lower specific energy consumption. Additionally, the proposed multi-objective optimization framework could be applied to other adsorbent materials and capture methods to guide the optimal design of CO_2/H_2O capture-based VAC systems for green building development.

Keywords

Carbon capture, multi-objective optimization, ventilation, air conditioning, green buildings, NSGA-II algorithm

The short version of the paper was presented at ICAE2022, Bochum, Germany, Aug 8-11, 2022. This paper is a substantial extension of the short version of the conference paper.

Nomenclature

Abbreviations

IAQ	Indoor air quality
VAC	Ventilation and air conditioning
ICC	Indoor CO_2 concentration
DAC	Direct air capture of CO_2
NSGA-II	Non-dominated sorting genetic algorithm-II
LDF	Linear Driving Force
RH	Relative humidity
VST	Vacuum solar thermal collectors
CHP	Combined heat and power
SCC	Specific cost of CO_2 avoidance

Variables

$\mathrm{AC}_{con}^{H_2O}$	Water dehumidification ratio of the conventional AC method
A_{STC}	The area of the rooftop solar thermal collector (m^2)
A_p	The contact area of water pipes and the adsorbent (m^2)
A_a	The contact area between feed air and the adsorbent (m^2)
$C_{\mathrm{H_2}O}$	Specific heat capacity of water at constant pressure (J/ (kg K))
$C_{p(a)}$	Specific heat capacity of solid adsorbent (J/ (kg K))
$C_{p(i)}$	Specific heat capacity of different gas species (J / (kg K))
$C_{p,a}$	Specific heat capacity of ambient air (J/ (kg K))
$C_{p,j}$	Specific heat capacity of air stream *j* (J/ (kg K))
E_{save}	The saved energy amount (J)
E_{AC}	AC energy consumption (J)
E_{reg}	Regeneration energy consumption (J)
h_{air}	The convective heat transfer coefficient of air
m_{CO_2}	Captured CO_2 mass (kg)
$\dot{\mathrm{m}}_j^i$	The mass flow rate of gas species in each gas stream *j* (kg/s)
$\dot{m}_f$	The mass flow rate of feed air (kg/s)
m_a	The sorbent mass (kg)
m_0^i	The equilibrium adsorption amount of gas *i* (mol/kg)
M^i	The molar mass for each gas species (kg/mol)
m_{room}^{air}	The air mass inside the room (kg)
m_t	Sorbent material type
m_{tank}	The mass of the hot water tank (kg)
$m_{room}^{\mathrm{H_2}O}$	The vapor mass inside the room (kg)
$n_{in/out}$	The molar number of inlet/outlet gas species (mol)
P_j^i	The partial pressure of each gas species in each gas stream (Pa)
$\dot{P}_j^i$	Real-time increment of partial pressure (Pa)
P_{amb}	The ambient pressure (Pa)
Q_v	The enthalpy of water evaporation (kJ/kg)
Q_s	Solar input (W)
Q_w	Heat collected by flowing water (W)
Q_r	Radiative heat loss (W)
Q_{reg}	Consumed regeneration heat (W)

The short version of the paper was presented at ICAE2022, Bochum, Germany, Aug 8-11, 2022. This paper is a substantial extension of the short version of the conference paper.

Q_A	Convective heat transfer from the flue gas during adsorption (W)
Q_h	Isosteric heat from adsorption/desorption reaction (W)
Q_{AC}^{con}	The total cooling demand required by conventional methods (W)
Q_{la}^{con}	The conventional latent load (W)
Q_{se}^{con}	The conventional sensible load (W)
Q_{AC}^{new}	The total cooling demand required by the proposed method (W)
$Q_{la(j)}^{new}$	The proposed latent load of air stream *j* (W)
$Q_{se(j)}^{new}$	The total proposed sensible load of air stream *j* (W)
Q_{all}^{new}	The total cooling demand required by the proposed method (W)
RH	Real-time RH inside the room
T_{CC}	Instantaneous chamber temperature (℃)
T_{reg}	Regeneration temperature (℃)
T_j	The temperature of air stream *j* (℃)
T_{ad}	The given adsorption temperature (℃)
T_{amb}	Ambient temperature (℃)
T_{room}	The room temperature (℃)
T_{in}	The inlet water temperature of solar thermal collectors (℃)
T_{out}	The outlet water temperature of solar thermal collectors (℃)
W_{Min}	Minimum work requirement for CO_2 capture(W)
X_{Q_s}	Total solar exergy input
X_{Q_w}	Total collected exergy by flowing working fluid
X	Time-averaged solar exergy input
x_i^i	Mass fraction of gas *i* in air stream *j*

Greek Letters

ω_i	The humidity ratio of different scenarios (kg/kg)
ω	Adsorbent thermal conductivity (W/m K)
ε	Adsorbent bed porosity
$\rho_r^{H_2O}$	The water vapor density inside the room (kg/m^3)
ρ_r^{air}	The humid air density inside the room (kg/m^3)
$\rho_b^{H_2O}$	Water vapor density of the returned gas (kg/m^3)
ρ	Crowdedness of the room (occupants/m^2)
ρ_s	Adsorbent density (kg/m^3)
ρ_p	Adsorbent particle density (kg/m^3)

Constants

Ideal gas constant R= 8.314472 (J/ (mol K)

Stephan Boltzmann Constant $\sigma = 5.67 \times 10^{-8}$ （W/ (m^2 K^4)

The short version of the paper was presented at ICAE2022, Bochum, Germany, Aug 8-11, 2022. This paper is a substantial extension of the short version of the conference paper.

1. Introduction

In the context of global efforts to realize carbon neutrality [1], achieving green buildings [2] has attracted growing attention owing to their merits of good indoor air quality(IAQ), energy-saving, and low CO_2 emission [3]. Yet, it remains a 'hard-to-achieve' target for traditional strategies relying on natural/mechanical ventilation, imposed by inherent conflicts between these merits. Specifically, maintaining a plausible IAQ requires timely removal of respiratory CO_2, which otherwise would rapidly accumulate to a level that causes adverse health impacts to occupants [4]. However, removing CO_2 from crowded indoors via traditional ventilation inevitably increases the air exchange rate with the ambient [5], inducing more energy consumption for air conditioning (AC) and thus CO_2 emission [6]. This dilemma is further exacerbated in hot and humid regions with extremely high latent and sensible loads of ambient air. A potential solution to this dilemma is to develop a new energy-efficient ventilation and air conditioning (VAC) system that can remove indoor CO_2 without increasing the air exchange rate. Adsorption-based direct air carbon capture (DAC) technology emerges as a promising candidate because it can directly and effectively remove CO_2 from the atmosphere [7]. At the same time, it is expected to perform better in stale indoor air environments featuring sub-ambient temperature and above-ambient CO_2 concentration.

Recent years have witnessed extensive efforts to demonstrate the feasibility of DAC technologies for indoor air treatment [8], with a particular interest in performance enhancement. One research route is to enhance CO_2 removal capacity by developing robust sorbent materials, especially under humid conditions. For example, Park et al. [9] synthesized new MOF-Polymer composite beads to achieve stable CO_2 adsorption capacity in humid indoor scenarios, realizing over 1-month lifetime without structural collapse. Lee et al. [10] developed a liquid-like CO_2 adsorbent made of carbon nanotubes and depicts 95% of initial capacity after 20 adsorption-desorption cycles. Being modified with hydrophobic coating, Zeolite 13X's CO_2 selectivity over H_2O was increased by 33.3% [11]. Besides, S. Kim et al. developed a structurally stable nano-encapsulated sodium hydroxide solvent [12] that achieved a high CO_2 capacity of 7.57 mmol/g for indoor capture. Using facile spray coating, Chae et al. [13] fabricated diamine-appended MOF composites that displayed invariant CO_2 capture capacity over 10 cycles when captured from indoor air with 60% RH. Despite their attempts to mimic the indoor conditions during performance determination, these experimental investigations were conducted under an insulated or constant environment, failing to capture the dynamic characteristics in the real world.

Another research route is to explore the energy-saving potential of the DAC-based system. M. Kim et al. [14] developed a CO_2 adsorption-based ventilation model and 30% of AC cooling energy in tropical summer and 60% of heating energy in Central European winter could be saved. Similarly, J. Harrouz et al. [15] applied MOF-based indoor carbon capture for a classroom and residential house, saving AC energy by 30% and 24%, respectively. Combining experiment and theoretical methods, L. Baus et al. [16] developed a DAC-based heating, ventilation, and air conditioning system (HVAC) and achieved energy-saving potentials higher than 37% in different scenarios. Lately, by adopting selective recirculation of post-captured air, we achieved a 43.57% of energy-saving potential in Hong Kong summer [17]. More recently, we have taken into account indoor vapor and conducted a global performance analysis on a solar-driven CO_2/H_2O capture system to demonstrate its feasibility in cities featuring distinct solar irradiation, temperature, and relative humidity [18].

Despite the extensive progress, most studies tend to separately optimize one performance by assuming the other is invariant. This might be impractical because the multiple performances of the whole system are not independent but interwoven or even conflicting. As a result, potential trade-offs might exist between the goals of CO_2 capture performance, energy-

The short version of the paper was presented at ICAE2022, Bochum, Germany, Aug 8-11, 2022. This paper is a substantial extension of the short version of the conference paper.

saving potential, and good IAQ. Such trade-offs are collectively dictated by external ambient environments (e.g., RH, temperature) and internal system configurations such as adsorbent materials. For example, RH has unignorable impacts on CO_2 adsorption capacity [19] and AC energy consumption [20]. Adsorbent materials play a core role in techno-energetic performance. As the benchmark [21] and most widely-used adsorbent for DAC [22], Zeolite 13X and Mg-MOF-74 depict differently in capacity, stability [23], hydrophilicity [24], and regeneration energy requirement [25], all of which may render these sorbents dissimilar biases on performances and thus application scenarios.

Solving these substantial uncertainties is pivotal yet challenging, which indispensably calls for a comprehensive evaluation to chart a wide range of key parameters. The parameters should cover system configurations, indoor conditions, and adsorbent characteristics. More importantly, their effects on different objectives should be unveiled, and objectives should be optimized based on practical constraints. One appropriate approach to orchestrate these complex requirements is the Non-dominated Sorting Genetic Algorithm II (NSGA-II), a mature algorithm that has been widely used to solve large-scale engineering problems with multiple conflicting and constrained objectives [26]. Specifically, it generates non-dominated and well-distributed Pareto solutions by applying ranking and elitism selection in parent and offspring populations [27]. Abundant studies have demonstrated its effectiveness in solving CO_2 capture-related applications, including achieving the maximum removal efficiency of CO_2 adsorption [28, 29], optimizing the thermo-economic performance of a CO_2 capture-integrated combined heat and power (CHP) system[30], and techno-economic performance for a CO_2 capture and utilization system [31].

Herein, this study develops an NSGA-II-based modeling-optimization framework for a dynamic solar-driven indoor CO_2/H_2O capture-based ventilation and air-conditioning system (IC-VAC), with the aim of maximizing both CO_2 capture performance and AC energy-saving potential. The proposed framework translates the green building's merits, i.e., high IAQ, low carbon emission, and low energy consumption into five constrained objectives, which are dictated by eight parameters, with the adsorbent type being one of them. Integrating the Quasi-Newtonian solver and NSGA-II algorithm, this framework optimizes the five objectives and, at the same time, compares the optimization behaviours between different adsorbents. Further, the mutual relationship between optimized objectives and decision parameters is articulated in a full-picture demonstration, in which the objectives of maximizing CO_2 removal capacity and minimizing AC energy consumption depict obvious trade-offs. Focusing on these conflicting objectives, dual-objective optimizations are further conducted to unveil the underlying mechanisms. To explain the difference between different adsorbents, their morphology variations after multiple cycles of CO_2 capture have been visualized by using scanning electron microscope (SEM). The remaining sections are structured as below. Section 2 describes the details of the simulation-optimization framework, in which the relationships between objectives and parameters are formulated. Section 3 validates the CO_2/H_2O isotherm models and the reliability of the NSGA-II algorithm. Section 4 presents the main results, discusses the adsorbent stability and economic feasibility, and compares the performance with other literature. Section 5 concludes this research.

The short version of the paper was presented at ICAE2022, Bochum, Germany, Aug 8-11, 2022. This paper is a substantial extension of the short version of the conference paper.

2. Concept and structure

The concept of a solar-driven indoor CO_2/H_2O capture-based ventilation and air conditioning system (IC-VAC) is shown in Figure 1(a), which is mainly based on the authors' previous work [17, 18]. This proposed solar-driven IC-VAC system consists of an array of rooftop vacuum solar thermal collectors (VST), a buffer tank for thermal energy storage, an adsorption-based CO_2/H_2O capture device, and a crowded building (schools, conference halls, concert halls, etc.) with an AC system. As shown in Figure 1 (a), the CO_2/H_2O-rich stale indoor air is introduced to the adsorption chamber, where CO_2 or H_2O molecules are captured at varied extents by the adsorbents. The post-captured air that features sub-ambient CO_2 concentration and RH is selectively recirculated instead of being discharged to the ambient air. By doing so, only a tiny stream of fresh air needs to be introduced into the room, to replenish respiration-consumed oxygen. Notably, the quality of post-capture air decreases because the adsorption process continuously degrades in nature [17]. At the near end of the adsorption, the post-captured air's CO_2 concentration might be too high, e.g.,> 80 Pa (selected by an electronic valve V_e in both Figure 1 (a) and (b)), and thus not suitable to be returned. In this case, it would be rejected to the ambient, and for maintaining the indoor pressure, a stream of fresh ambient air with the same mass flow rate would be supplied. During desorption, rather than consuming grid power to heat the adsorbents, this study leverages renewable solar thermal energy obtained by V-STC, which can achieve temperatures of around 100°C [32], sufficient for the regeneration of the DAC system, e.g.,> 70 °C. To effectively regulate the above process for maximizing CO_2 removal performance and minimizing AC energy-saving, a feasible energy-mass management strategy that covers all the subsystems should be developed via multi-objective optimization that charts a wide range of parameters, which is depicted in the next section.

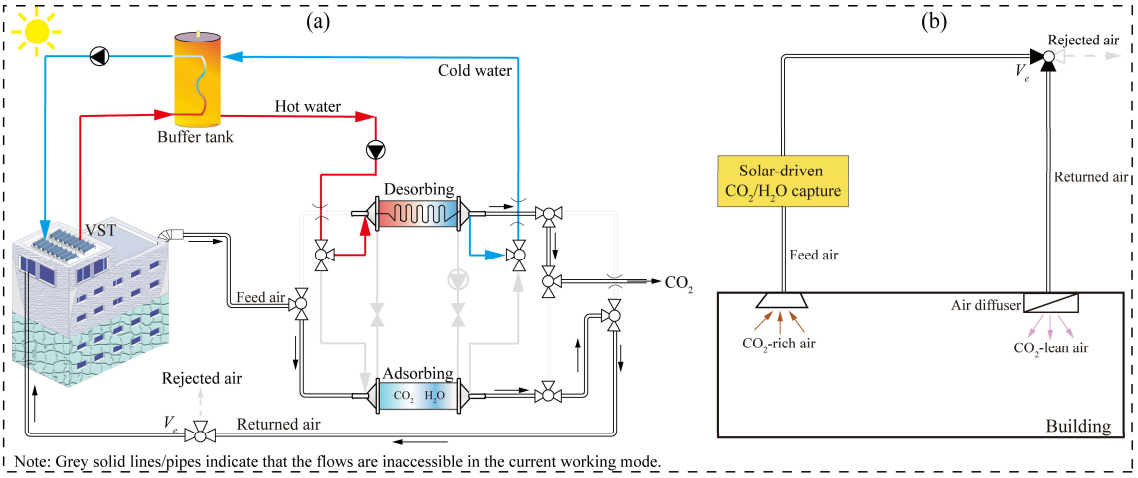

Figure 1. The paradigm of the proposed solar-driven indoor CO_2/ H_2O capture-based ventilation and air conditioning (IC-VAC) system: (a) the overall conceptual diagram; (b) a detailed portrait of air recirculation.

2.1 Objectives simulations

Figure 2 (a) charts eight decision variables (x_1-x_8 in Eq.(1)) from all subsystems and five key objectives (Z1-Z5) that are mapped from the three merits of green building in Figure 2 (b). Specifically, the "Indoor air quality" merit is reflected by Z1-indoor CO_2 concentration and Z2-indoor RH level; the "CO_2 capture capacity" merit is evaluated based on objectives Z3-captured CO_2 amount; and the "Energy-efficient" merit is evaluated by Z4-overall energy-saving potential and Z5-overall exergy efficiency. The input layer of the combined Quasi-Newtonian solver and NSGA-II algorithm [33, 34] framework is generated by variables x_1-x_8

The short version of the paper was presented at ICAE2022, Bochum, Germany, Aug 8-11, 2022. This paper is a substantial extension of the short version of the conference paper.

that randomly take values from their defined. The combined modeling-optimization framework keeps iterating for different input layers until the NSGA-II finds its Pareto fronts (PF). Based on the same saturation limit of 80%, the Pareto fronts are expected to simultaneously minimize their VAC energy consumption, maximize the CO_2 removal capacity, and maintain indoor comforts without decreasing exergy efficiency.

$$\mathrm{X} = [x_1\ x_2\ x_3\ x_4\ x_5\ x_6\ x_7\ x_8]^T \tag{1}$$

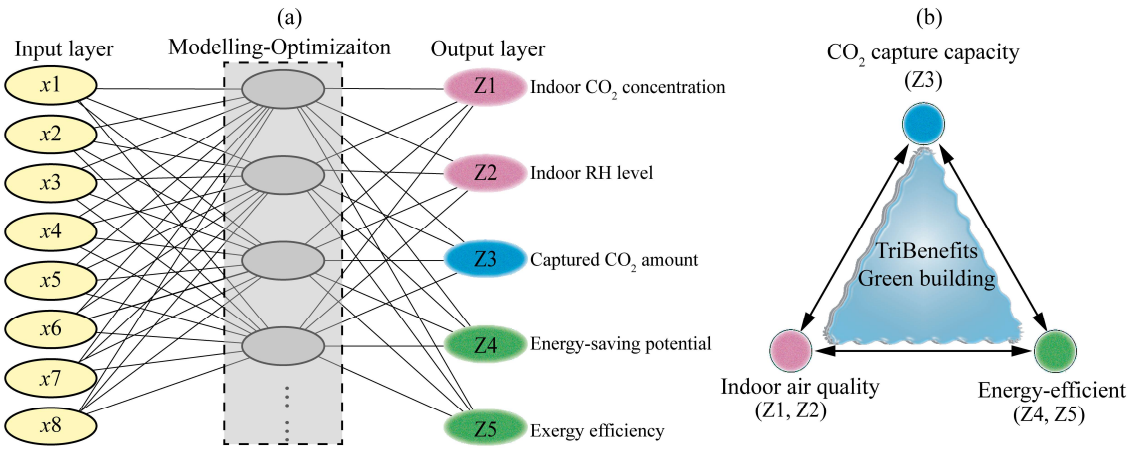

Figure 2. Schematic of the combined modeling-optimization process: (a) the 3-layer illustration that covers the decision parameters and five key objectives; (b) demonstration of modern green buildings' triple benefits, in which exergy efficiency and energy-saving potential are categorized into the benefit of "Energy-efficient'.

The definitions of variables, objectives, and constraints are enlisted in Table 1. For example, x_1 is the mass flow rate of the feed air $\dot{m}_f$ that determines the working load of the capture device; x_2 is the occupancy of the indoor environment ρ that reflects the crowdedness levels. x_3, x_4 are ambient RH and temperature, associated with the latent and sensible loads of AC; x_7 is the hourly mean solar irradiance Irr, which decides the amount of solar thermal input of the integrated system; x_8 is the sorbent material type, including Zeolite 13X (shortened as 13X) and Mg-MOF-74 (shortened as MOF), which display different characteristics of CO_2/H_2O affinity, energy intensity, and cyclability. To conduct optimization in practical manners, six constraints are applied: (1) objective Z1 should always be lower than the upper limit of harmless air (i.e., < 100 Pa); (2) Z2 should be in the comfortable range of 25%~60%; (3, 4) Objectives Z3 and Z4 should be positive values; (5) The overall exergy efficiency Z5, related to the initial solar exergy input, should be higher than 2% to avoid massive energy loss issues; (6) All adsorption processes must satisfy the unified saturation limit of 80%.

Table 1. Detailed illustrations of studied variables and optimized objectives in this study.

Variables	Description	Lowest bound	Highest bound	Units
x_1, $\dot{m}_f$	Feed air mass flow rate	0.1	1.5	kg/s
x_2, ρ	Occupancy	0.2	1.4	occupants/m^2
x_3, RH	Outdoor relative humidity	5	90	%
x_4, T_{amb}	Outdoor temperature	25	32	°C
x_5, P_{lim}	CO_2 pressure limit	40	100	Pa
x_6, m_a	Total sorbent mass	2000	36000	kg
x_7, Irr	Solar irradiation	50	1000	W/m^2
x_8, m_t	Sorbent material type	Zeolite 13X	Mg-MOF-74	
Objectives	Description			
Z_1	Indoor CO_2 concentration			
Z_2	Indoor relative humidity			

The short version of the paper was presented at ICAE2022, Bochum, Germany, Aug 8-11, 2022. This paper is a substantial extension of the short version of the conference paper.

Z_3	Captured CO_2 mass
Z_4	Energy-saving percentage
Z_5	Exergy efficiency

Constraints	Description
c_1	Z_1 < 100 Pa, to ensure the indoor air quality
c_2	25% < Z_2
c_3	Z_2 <60%
c_4	Z_3 should be higher than the total respiratory CO_2 amount
c_5	Z_5 > 2%, subjecting to total incident solar irradiation
c_6	Saturation limit during adsorption = 80%

2.2 NSGA-II based multi-objective optimization flow chart

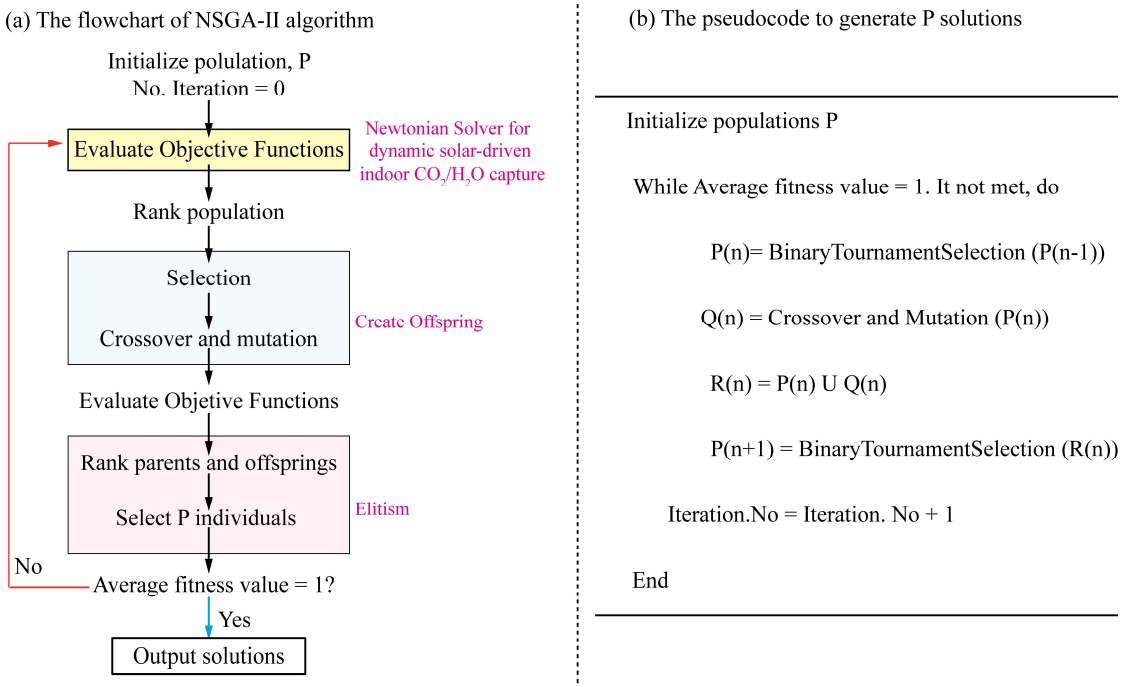

Figure 3. (a) The flowchart of integrated Quasi Newtonian solver-NSGA-II optimization process; (b) the pseudocode to generate the Pareto front solutions.

Figure 3 shows the flowchart of the NSGA-II algorithm based on the concept of Pareto dominance. The working process mainly includes three steps. First, the algorithm creates a stochastic initial population of candidate solutions P (as shown in Figure 3 (a)), which are evaluated individually subjecting to the objective functions. Based on Pareto dominance, these solutions are ranked by calculating their crowding distance in the non-dominated front. Based on their ranking and crowding distance, a subset of solutions is selected to create the next generation Q (Figure 3 (b)). Then, genetic operators such as crossover and mutation are applied to generate a new population of candidate solutions R. Finally, the algorithm terminates if the given termination criterion is met, which in this study, is "average convergence value = 1". If not, return to the evaluation step. The final output is a collection of non-dominated solutions, also known as the Pareto fronts, which represent the optimized trade-off between multiple conflicting and constrained objectives.

The short version of the paper was presented at ICAE2022, Bochum, Germany, Aug 8-11, 2022. This paper is a substantial extension of the short version of the conference paper.

2.2.1 Objective 1—Indoor CO_2 concentration

Low CO_2 emission and satisfactory IAQ (objective 1) are the prominent features of green buildings, and the dynamic indoor CO_2 concentration $P_{room}^{CO_2}(t)$ (Pa) is calculated as below:

$$P_{room}^{CO_2}(t) = P_{room}^{CO_2}(t-1) + \dot{P}_{in}^{CO_2}(t) \tag{2}$$

where $\dot{P}_{room}^{CO_2}(t)$ is the instant variation of the indoor CO_2 concentration, further represented by:

$$\dot{P}_{in}^{CO_2}(t) = \frac{\sum_1^j (x_j^{CO_2} \times \dot{m}_j^{air}) \times dt / M^{CO_2}}{m_{room}^{air}(t)/M^{air}} \times P_{atm} \tag{3}$$

here $x_j^{CO_2}$ and $\dot{m}_j^{air}$ are the mass fraction of CO_2 and mass flow rate of different air streams j, respectively. j includes feed air stream, captured stream, recirculated stream, and newly-injected stream. The mass balance is explained in detail in the authors' previous work [17]. M^{air} and M^{CO_2} are the molar mass of air (0.0029 kg/mol) and CO_2 (0.044 kg/mol), respectively. P_{atm} is one atmosphere, 1.013×10^5 Pa. And $x_j^{CO_2}$ can be calculated as below:

$$x_j^{CO_2} = \frac{M^{CO_2} \times P_j^{CO_2}}{M^{air} \times P_{atm}} \tag{4}$$

here $P_j^{CO_2}$ is the partial pressure of CO_2 in air stream j.

$$P_j^{CO_2} = \begin{cases} \dfrac{\dot{m}_j^{CO_2}/M^{CO_2}}{\dot{m}_j^{air}/M^{air}} \times P_{atm}, mode\ 1 \\ 40, \quad mode\ 2 \\ 40, \quad mode\ 3 \end{cases} \tag{5}$$

The daily mean value of $P_{room}^{CO_2}(t)$ is treated as objective 1, Z_1, ICC, in the following NSGA-II optimization process. Here, t_{max} is the end simulation time of the day (19:00); while t_{min} is the start simulation time (7:00), and dt is the simulation time step (30 s).

$$Z_1, ICC = \int_{t_{min}}^{t_{max}} P_{room}^{CO_2}(t)dt / (t_{max} - t_{min}) \tag{6}$$

2.2.2 Objective 2—Indoor RH level

Objective 2, referred to the daily mean value of indoor RH, can be obtained by:

$$Z_2, IRH = \int_{t_{min}}^{t_{max}} IRH(t)dt / (t_{max} - t_{min}) \tag{7}$$

where $IRH(t)$ is the real-time variation of indoor RH, an important indicator of thermal comfort.

$$IRH(t) = CoolProp\_HAPropSI(T_{room}(t), P_{amb}, \omega_{room}(t)) \tag{8}$$

It can be evaluated based on the humidity ratio inside the room, ω_{room}, by an open-source database, CoolProp [35]. T_{room} represents the room temperature (K).

$$\omega_{room}(t) = \frac{m_{room}^{H_2O}}{m_{room}^{air} - m_{room}^{H_2O}} \tag{9}$$

ω_{room} is calculated by Eq. (9), where $m_{room}^{H_2O}$ and m_{room}^{air} are the total mass of water vapor and air inside the room, respectively.

$$m_{room}^{H_2O} = m_{room}^{H_2O}(t-1) + \dot{m}_{room}^{H_2O}(t) \tag{10}$$

here $\dot{m}_{room}^{H_2O}(t)$ is the instant increment of water vapor amount inside the room, which is the net water vapor variation and is calculated below:

$$\dot{m}_{room}^{H_2O}(t) = \dot{m}_{re}^{H_2O} + \dot{m}_a^{H_2O} - \dot{m}_{fe}^{H_2O} - \dot{m}_{AC}^{H_2O} \tag{11}$$

The short version of the paper was presented at ICAE2022, Bochum, Germany, Aug 8-11, 2022. This paper is a substantial extension of the short version of the conference paper.

The real-time increment of water vapor amount in each j air stream can be calculated as below:

$$\dot{m}_j^{H_2O} = (\dot{m}_j^{air} - \dot{m}_j^{H_2O}) \times \omega_j \quad (12)$$

where ω_j is the humidity ratio. More details can be found in the authors' previous work [18].

$$P_{room}^{H_2O} = CoolProp\_HAPropSI(T_{room}(t), P_{amb}, RH(t)) \quad (13)$$

2.2.3 Objective 3—Captured CO_2 mass

The captured CO_2 mass of the proposed system largely depends on the used sorbent materials. Table 2 shows the detailed characteristics of the two sorbent materials, i.e., 13X and MOF, and Table 3 shows the isotherm model coefficients. The sorbents' real-time uptakes of CO_2/H_2O (adsorption kinetics) $\dot{m}_c^i$ can be described by the Linear Driven Force model [19, 36]:

$$\dot{m}_c^i = k^i \times (m_0^i - \mathrm{m}_c^i) \quad (14)$$

where k^i are the adsorption time constant of CO_2 and H_2O, respectively, (s^{-1}), related to the adsorbents' particle sizes, porosity, etc.; m_0^i are the equilibrium adsorption amount of CO_2 and H_2O (mol/kg) obtained by leveraging the Langmuir adsorption isotherm model [37] and m_c^i (mol/kg) denotes the actual adsorbed amount.

$$m_0^i = m_0 \times \frac{K \times P_{room}^i}{1 + K \times P_{room}^{\mathrm{i}}} \quad (15)$$

here m_0 and K are the empirical constants of the adsorption kinetics of each gas species [17]. The total amount of daily captured CO_2 is considered as objective 3.

$$Z_3, m_{CO_2} = M^{CO_2} \times \int_{t_{min}}^{t_{max}} \dot{m}_{CO_2}(t)dt \quad (16)$$

Another important index here is the purity of the collected CO_2, which is defined below, with $\sum_1^i \mathrm{m}_c^i$ being the amount of total captured gases (kg). The purity index is strictly observed and regulated above 80% throughout the entire simulation.

$$purity = \frac{Z_3, m_{CO_2}}{\sum_1^i \mathrm{m}_c^i} \quad (17)$$

Table 2. Adsorbed bed characteristics of Zeolite 13X and Mg-MOF-74.

Properties/ Materials	Zeolite 13X	Mg-MOF-74	Ref.
Adsorbent density, ρ_s	533.8 kg/m^3	230.1 kg/m^3	[19]
CO_2 adsorption heat, ΔH_{CO_2}	-30,731 J/mol	-42,000 J/mol	[38], [19]
N_2 adsorption heat, ΔH_{N_2}	-14,935 J/mol	-18,000 J/mol	[38], [19]
H_2O adsorption heat, ΔH_{H_2O}	-53,289 J/mol	-48,991 J/mol	[19], [39]
Particle density, ρ_P	1,230 kg/m^3	911 kg/m3	[19], [39]
Bed porosity, ε	0.566	0.7417	[19]
Inlet temperature, T_{ad}	297 K	297 K	[19], [39]
CO_2 LDF coefficient, K_{L,CO_2}	0.006 s^{-1}	0.1182 s^{-1}	[19]
H_2O LDF coefficient, K_{L,H_2O}	0.000058 s^{-1}	0.00123 s^{-1}	[19], [39]
sorbent specific heat capacity, $C_{p(sor)}$	900 J/ (kg K)	900 J/ (kg K)	[19], [39]
Adsorbent thermal conductivity, ω	0.2 W/ (m K)	0.3 W/ (m K)	[19], [39]
Particle size, D_p	0.0015 m	0.0002 m	[19], [39]

The short version of the paper was presented at ICAE2022, Bochum, Germany, Aug 8-11, 2022. This paper is a substantial extension of the short version of the conference paper.

Table 3. Isotherm models of Zeolite 13X and Mg-MOF-74.

Isotherm Parameters		q_m (mol/kg)	K_0 (Pa^{-1})	Ref.
Mg-MOF-74	CO_2	11.4048	$3.089e^{-11}$	[19]
	N_2	6.7072	$9.36e^{-10}$	[19]
	H_2O	48.35	$2.21e^{-9}$	[39]
Zeolite-13X	CO_2	9.842	$6.86e^{-9}$	[38]
	N_2	N/A	$8\times10e^{-10}$	[38]
	H_2O	15.4849	$1.68e^{-10}$	[19]

2.2.4 Objective 4—AC Energy-saving potential

Objective 4 is the energy-saving potential in an entire day compared to traditional ventilation methods, whose energy consumption is calculated below.

$$Q_{AC}^{con} = Q_{la}^{con} + Q_{se}^{con} \tag{18}$$

Q_{AC}^{con} is the total energy demand required by conventional ventilation approaches, in which the ambient air exchange rate is required for maintaining the same level of ICC as the new method. It comprises the latent heat demand Q_{la}^{con} and sensible heat demand Q_{se}^{con}.

$$Q_{la}^{con} = 1.2 \times \dot{m}_{con}^{H_2O} \times Q_v \tag{19}$$

Here, a compensation factor of 1.2 is assumed here to compensate for energy loss during the cooling process [16]. $\dot{m}_{con}^{H_2O}$ is the dynamic dehumidified water amount and Q_v is the enthalpy of water evaporation (2450 kJ/kg) [40]. $\dot{m}_{con}^{H_2O}$ can be calculated as below:

$$\dot{m}_{con}^{H_2O} = AC_{con}^{H_2O} \times (\dot{m}_{con}^{air} - \dot{m}_{con}^{H_2O}) \times \omega_a \tag{20}$$

where $AC_{con}^{H_2O}$ is a given ratio between the required amount of dehumidified water and water content in the newly introduced air. This coefficient is in accordance with the designed IAQ standard of 60% from EN 16798-1[41] and assumed a constant of 0.65 based on trial-and-error during the study. ω_a is the humidity ratio of the ambient air.

$$Q_{se}^{con} = \dot{m}_{con}^{air} \times C_{p,a} \times (T_{amb} - T_{room}) \tag{21}$$

Eq.(21) calculates the conventional sensible cooling energy demand, Q_{se}^{con}. Here, $C_{p,a}$ is the specific heat capacity of ambient air, T_{amb} and T_{room} are ambient temperature and room temperature, respectively.

$$Q_{AC}^{new} = \sum_1^j (Q_{la(j)}^{new} + Q_{se(j)}^{new}) \tag{22}$$

The AC energy demand of the proposed system, Q_{AC}^{now}, is calculated by Eq. (22), which also comprises the latent and sensible energy demands.

$$Q_{se(j)}^{now} = (\dot{m}_j^{air} \times C_{p,j}) \times (T_j - T_r) \tag{23}$$

$C_{p,j}$ is the specific heat capacity of any air stream j and is evaluated by CoolProp. Eq. (24) calculates the total energy consumption of the proposed scheme, incorporating the thermal energy consumed by CO_2/H_2O capture, Q_{reg}. Here, Q_{reg} affects the desorption temperature, which is directly related to the capture rate and purity of the adsorption process.

$$Q_{all}^{now}(t) = Q_{AC}^{now}(t) + Q_{reg}(t) \tag{24}$$

Q_{all}^{now} is the total energy demand for the proposed system that includes the thermal energy consumption by CCA's desorption process Q_{reg}.

$$E_{save} = \int_{t_{min}}^{t_{max}} Q_{AC}^{con} dt - \int_{t_{min}}^{t_{max}} Q_{all}^{now} dt \tag{25}$$

The short version of the paper was presented at ICAE2022, Bochum, Germany, Aug 8-11, 2022. This paper is a substantial extension of the short version of the conference paper.

E_{save} is the energy saved between conventional and proposed systems in a daytime simulation.

$$Z_4, \delta_{save} = \frac{E_{save}}{\int_{t_{min}}^{t_{max}} Q_{AC}^{con} dt} \times 100\% \tag{26}$$

Thereby, objective 4, δ_{save}, can be defined by Eq.(26).

2.2.5 Objective 5—Exergy efficiency

To evaluate the energy conversion performance of this system, exergy efficiency, defined as the ratio of ultimate useful CO_2 separation work over the input solar exergy, is incorporated as an objective. During optimization, this objective is constrained to be larger than a given value to guarantee the energy conversion efficiency of the solutions.

$$\left(m_{\mathrm{a}(\frac{1}{2})} C_{p(a)} + \sum_{i=1}^{3} \dot{m}_c^i(t) C_{p(i)} \right) \frac{dT_{CC}}{dt} = Q_A + Q_h + Q_{reg} \tag{27}$$

Eq. (27) describes the thermodynamic balance relationship of carbon capture. $m_{a(1/2)}$ is the mass of adsorbent material in each chamber (kg); $C_{p(a)}$ is the specific heat capacity of the adsorbent. $\dot{m}_c^i(t)$ and $C_{p(i)}$ are the captured gas flow rate and specific heat capacity of each gas. T_{CC} is the instant temperature inside the chamber. Q_A is the convective heat transfer from the feed air. Q_h is the isosteric heat from the adsorption heat. Q_{reg} is the thermal energy consumption by regenerating the saturated adsorbent material. These thermal sectors are calculated by Eq. (28) below, and more information can be referred to our previous works [17, 18].

$$\left\{ \begin{array}{c} Q_A = \begin{cases} h_{air} A_a (T_{ad} - T_{CC}), & \text{adsorption} \\ 0 & \text{otherwise} \end{cases} \\ Q_h = \sum_{i=1}^{3} \dot{m}_c^i(\mathrm{t}) \times \triangle H \\ Q_{reg}(t) = \begin{cases} k_{H_2O} A_p (T_{CC(2)}(t) - T_{CC(1)}(t)) & \text{Internal Heat exchange} \\ k_{H_2O} A_p \left(T_{reg}(t) - T_{CC}(t) \right) & \text{Desorption} \\ 0 & \text{adsorption} \end{cases} \end{array} \right\} \tag{28}$$

where h_{air} and k_{H_2O} are the convective heat transfer coefficient of air and water (J/(kg K), respectively, which are decided by their flow speeds. A_a is the contact area between the adsorbent material with the feed air and hot pipes (m^2), respectively. $T_{reg}(t)$ is the instant temperature inside the desorption (regeneration) chamber. T_{ad} is the adsorption temperature, which in this case, equals to the room temperature T_{room}.

$$\left\{ \begin{array}{c} T_{in}(t) = T_{reg}(t-1) \\ T_{reg}(t) = T_{reg}(t-1) + \frac{(Q_w(t) - Q_{reg}(t-1))}{m_t \times C_{H_2O}} \times dt \end{array} \right\} \tag{29}$$

T_{in} is the water inlet temperature, the same as the regeneration temperature from the last step. m_t is the working fluid mass inside the buffer tank (kg). Q_w is the useful thermal energy gain (W).

$$Q_s = Q_w + Q_r + Q_{\boldsymbol{c}} \tag{30}$$

Eq. (30) is the Frist thermodynamic law for energy conservation, which demonstrates the thermal balance equation of the vacuum solar thermal collector subsystem. Q_s is the total solar energy that sheds onto the thermal collector, while Q_w is the successfully collected solar heat by hot water; Q_r is the radiative heat loss, while the convective heat loss $Q_{\boldsymbol{c}}$ is neglected.

The short version of the paper was presented at ICAE2022, Bochum, Germany, Aug 8-11, 2022. This paper is a substantial extension of the short version of the conference paper.

$$\left\{\begin{array}{c} Q_s = G \times A_{STC} \times \alpha \\ Q_w = \dot{m}_{fluid} C_{fluid} \left(T_{reg} - T_{in}\right) \\ Q_r = \varepsilon_r \sigma A_{STC} (T_{STC}^4 - T_{sky}^4) \end{array}\right\} \tag{31}$$

where G is the total radiation summed by direct normal irradiance (DNI) and diffuse horizontal irradiance (W/m^2); A_{STC} defines the PV panel's surface area (m^2), the same as the simulated room size. α is the absorptivity of the PV cell; $\dot{m}_{fluid}$ is the mass flow rate of the working fluid, kg/s ; C_{fluid} is the specific heat capacity of the working fluid at constant pressure (J/(kg K); Below are the equations calculating useful solar exergy input. ε_r is the emissivity factor subject to the entire spectrum; σ is the Stephan Boltzmann constant; T_{sky} is the sky temperature obtained from [42]:

$$T_{sky} = \frac{1}{4} \varepsilon_{sky} \times T_{amb} \tag{32}$$

here ε_{sky} is the emissivity of the sky and is relevant to the dew point temperature and relative humidity in the ambient [43].

$$X_{Q_s} = Q_s \times (1 + \frac{1}{3} \times \left(\frac{T_{reg}}{T_{sun}}\right)^4 - \frac{4}{3} \times \frac{T_{reg}}{T_{sun}} \tag{33}$$

$$X = \int_{t_{min}}^{t_{max}} X_{Q_s}(t) dt \; / \; (t_{max} - t_{min}) \tag{34}$$

X_{Q_s} is the total solar exergy input, and X is the average value. T_{sun} is the temperature of the sun's photosphere (5778 K).

$$Z_5, \eta_{2nd} = \frac{W_{Min}}{X} \times 100\% \tag{35}$$

The solar-driven IC-VAC system's exergy efficiency η_{2nd} is defined as the ratio of the minimum separation work to time-averaged useful solar exergy input. W_{Min} is the minimum power requirement for CO_2 capture as elucidated by the Gibbs free minimum energy separation law [44], which can be calculated as below:

$$\begin{aligned} W_{Min} = RT_{amb} \Bigg[& n_{out} \sum_{i=1}^{3} y_{out(j)}(t) \log_e y_{out(j)}(t) + n_{waste} \sum_{i=1}^{3} y_{waste(j)}(t) \log_e y_{waste(j)}(t) \\ & - n_{in} \sum_{i=1}^{3} y_{in(j)}(t) \log_e y_{in(j)}(t) \Bigg] \end{aligned} \tag{36}$$

Here R is the ideal gas constant (8.314 J/mol K); n is the molar flow rate; y is the molar mass fraction. Subscripts of in, out, and $waste$ refer to the inflow flue gas, captured gas sample, and uncaptured gas streams. The ratio of $n_{out}^{CO_2}$ over $n_{in}^{CO_2}$ is defined as the capture rate in our simulation model. More modelling details regarding indoor mass conservation, CO_2 capture and solar thermal system can be found in our previous publications [17, 43].

3. Validations

Considering the governance on the techno-energetic performance, the CO_2/H_2O capture capacity of both adsorbent materials should be verified based on the CO_2 and H_2O's adsorption isotherms. Typically, the adsorption isotherm of a solid adsorbent material refers to the relationship between the amount of CO_2/H_2O it uptakes and partial pressures at a given temperature. By setting the same adsorbent properties and working temperature (298 K) as the reference experiment, fair comparisons can be made to validate the proposed CO_2/H_2O capture models.

The short version of the paper was presented at ICAE2022, Bochum, Germany, Aug 8-11, 2022. This paper is a substantial extension of the short version of the conference paper.

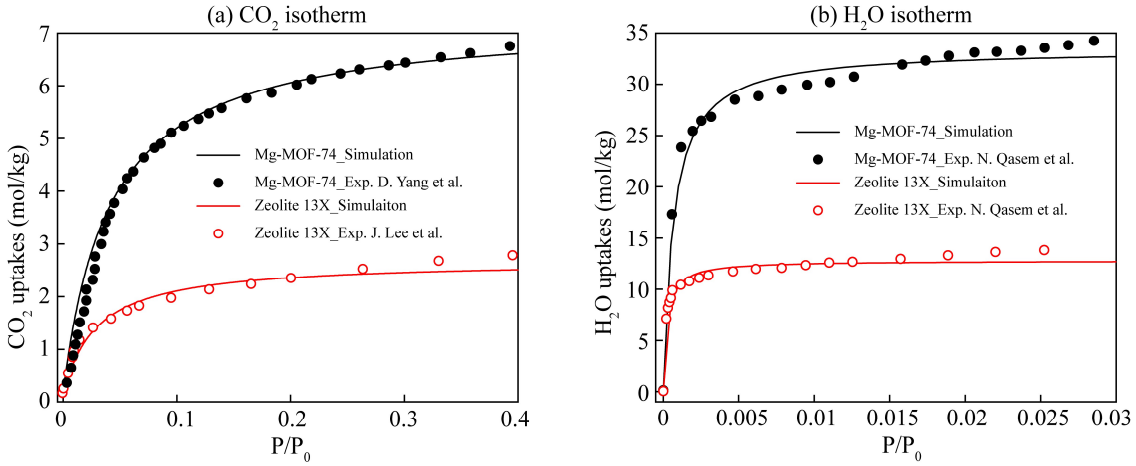

Figure 4. Validation of isotherm models of MOF and 13X by comparisons with experimental data: (a) CO_2 isotherm; (b) H_2O isotherm.

Specifically, Figure 4 (a) validates the predicted CO_2 isotherm against the experimentally measured results of MOF [45] and 13X [46] at 298 K, under varying partial pressure P/P_0, with the average errors of 8.57% and 8.42%, respectively. Such discrepancies could be attributed to numerical approximations and ideally non-fluctuated temperature conditions in simulation models. Figure 4 (b) validates the H_2O isotherm of both MOF and 13X against the experimental results from [39] at an adsorption temperature of 298 K. The corresponding average errors are 3.3% and 2.8%, respectively, demonstrating great agreement. According to the isotherm results, MOF tends to have a higher uptake capacity for CO_2 and H_2O than 13X. This advantage may change in the later simulations because the adsorbed H_2O affects CO_2 capture at varied extents for different adsorbent materials.

The commonly used indicator to validate that all the obtained solutions from the last iterations are the desired Pareto fronts is the average non-domination fitness value. It varies with the iteration number and will approach the value of 1 when the iteration converges and locates the Pareto front solutions. The fitness value has to be validated for each optimization procedure, to prove that each solution in the final population is at the extent to which it cannot further improve one objective without worsening another objective [47]. To this end, Figures 5 (a)-(c) present the average fitness value variation for 3 different optimization procedures conducted in this research. They all achieved a fitness value of 1, indicating the optimized solutions we obtained are Pareto fronts.

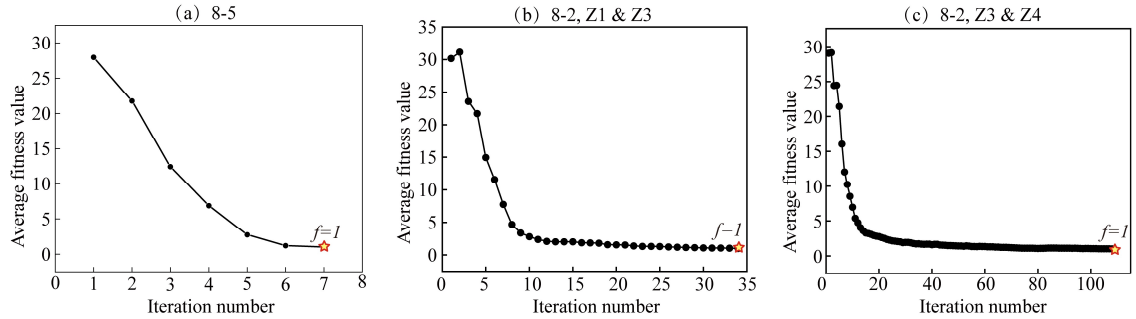

Figure 5. Average non-domination convergence plot after each iteration, based on 8 variables: (a) optimizing 5 objectives; (b) dual-objective between objectives 1 and 3; (c) dual-objective between objectives 3 and 4.

4. Results and discussions

This section starts by comparing the real-time ICC variation and energy consumption between 13X and MOF in Figure 6, to lay the groundwork for analysing their distinct

The short version of the paper was presented at ICAE2022, Bochum, Germany, Aug 8-11, 2022. This paper is a substantial extension of the short version of the conference paper.

behaviours in the following sections. Specifically, sub-section 1 unveils the interactions among all 5 objectives of both adsorbents, with the dominant decision parameter being probed. Sub-section 2 depicts the trade-off between minimizing ICC and maximizing m_{CO_2}. Sub-section 3 shows the trade-off between maximizing CO_2 capture amount and maximizing energy-saving potential.

Table 4. The dynamic performance in one day between Zeolite 13X and Mg-MOF-74.

Material	Z1	Z2	Z3	Z4	Z5	E_{AC}	E_{reg}	Purity
13X	89.65	46%	89.52	0.3297	7.4	72.86	133.68	95.81%
MOF	61.97	28%	92.75	0.2332	4.53	70.61	162.19	84.53%

Figure 6 presents the dynamic ICC variation and thermal energy consumption Q_{reg} for 13X and MOF, with daily average results shown in Table 4. In Figure 6 (a), when satisfying ICC < 100 Pa, MOF has a higher CO_2 capture capacity than 13X. The total captured CO_2 mass and average ICC per day for MOF is 92.75 kg and 61.97 Pa, 3.5% higher and 45.2% lower than 13X. Notably, ICC shows a rapid increase at the end of each cycle for both materials, resulting from a short pause of adsorption that occurs when two chambers exchange heat internally. According to Figure 6 (b), MOF desorbs faster and undergoes one more cycle than 13X in one day, resulting in more total thermal consumption E_{reg}. By contrast, the two materials show comparable energy consumption for air conditioning E_{AC}, because E_{AC} is mostly decided by the exchange rate with the ambient rather than adsorbents. Compared to 13X, MOF can capture more CO_2 and maintain a lower indoor RH level because of its higher H_2O affinity, which would adversely influence the purity of captured CO_2. According to Table 4, MOF achieves a purity of 85.53%, lower than 95.81% for 13X.

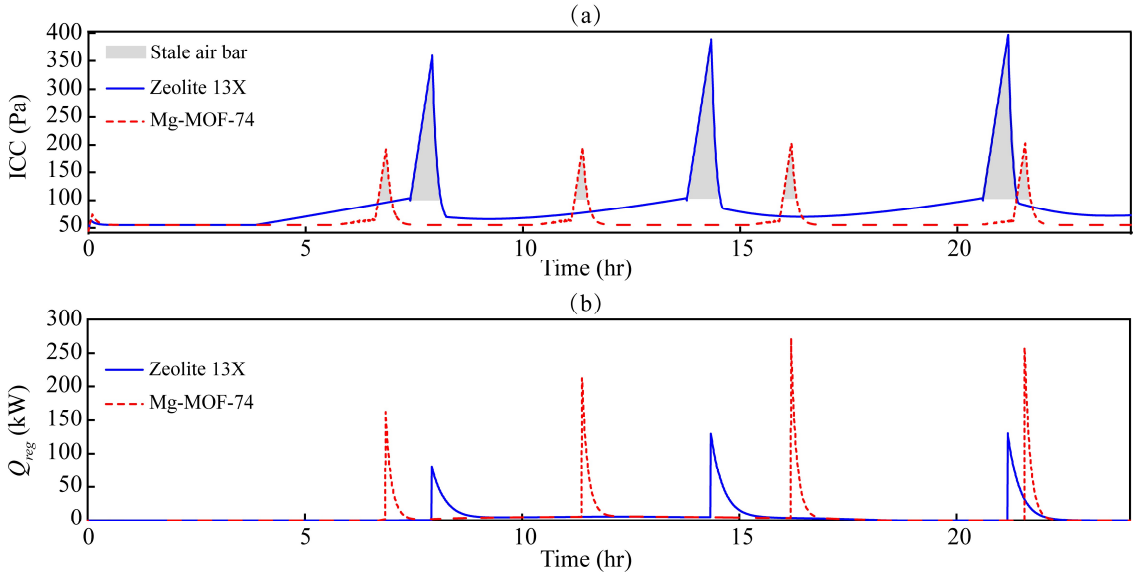

Figure 6. Real-time performance comparisons between two different sorbent materials, Mg-MOF-74 and Zeolite 13X. (a) Indoor CO_2 concentration, with above-limit sections shaded in different colours; (b) Regeneration heat consumption. The other working conditions are identical: m_a = 3700 kg, $\dot{m}_f$ = 0.68 kg/s, ρ = 0.5 occupants/m^2.

4.1 Correlation analysis among 5 optimized objectives

As a preliminary, the interactions among five optimized objectives are presented to locate the conflicting objective pairs in Figure 7. Specifically, the full-picture optimization is conducted based on eight decision parameters, with the adsorbent material type being one of them. For both adsorbents, IRH shows no obvious interaction with ICC in Figure 7 (a), as it is

The short version of the paper was presented at ICAE2022, Bochum, Germany, Aug 8-11, 2022. This paper is a substantial extension of the short version of the conference paper.

constrained by c_2 and c_3 and solely decided by the ambient RH (according to Figure 8 (b)). However, as depicted in Figure 7 (b), a higher IRH is observed to conflict with m_{CO_2} for MOF, whose CO_2 capacity has a lower tolerance of moisture. On the contrary, in Figure 7 (c), a higher IRH shows a positive impact on improving δ_{save}, due to a higher extent to which the latent load can be reduced.

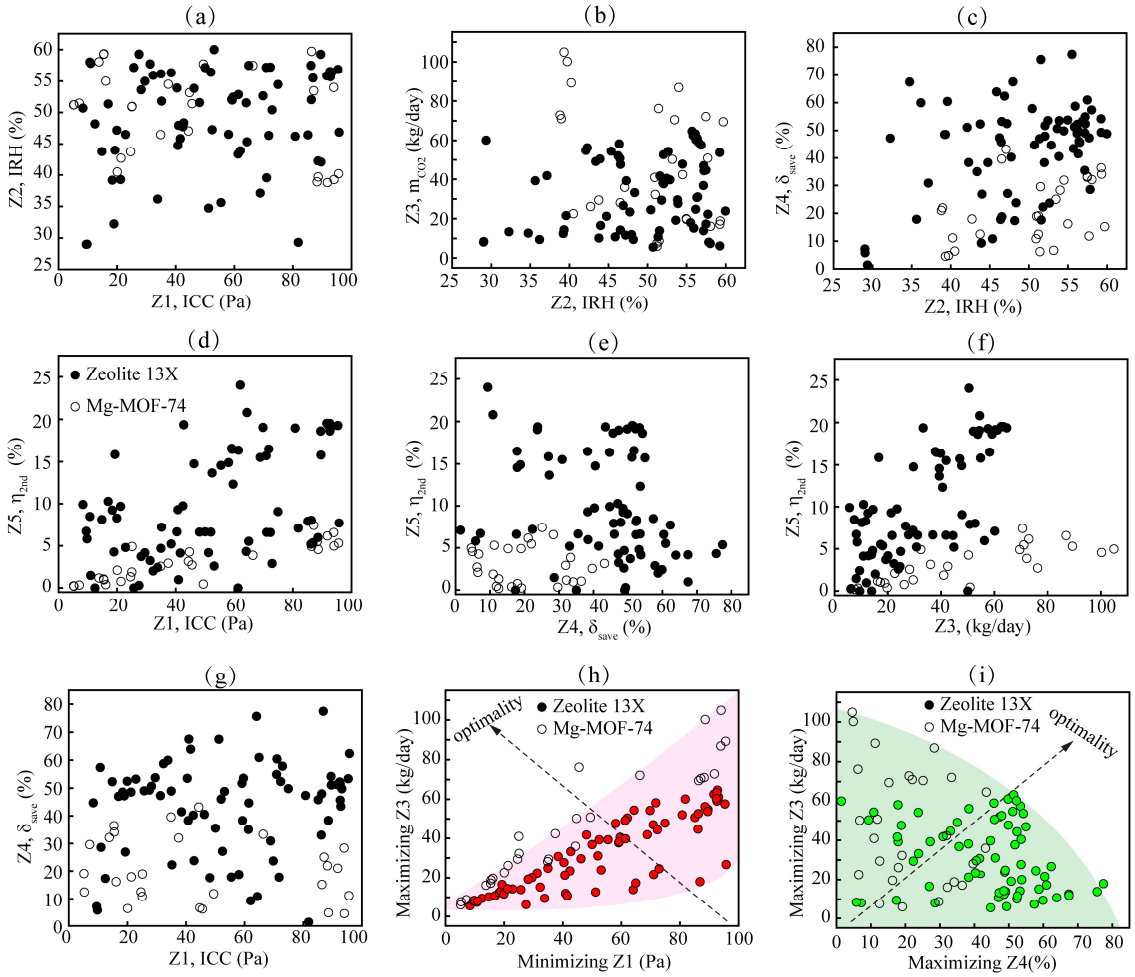

Figure 7. Constrained optimized results for Zeolite 13X and Mg-MOF-74 while optimizing 5 objectives altogether: (a)-(g) mutual interactions between different pairs of objectives; (h) trade-off between minimizing Z1 and maximizing Z3; (i) trade-off between maximizing Z3 and maximizing Z4.

Moreover, according to Figure 7 (d) - (f), MOF solutions have 70% lower exergy efficiency than 13X, owing to higher energy requirement during the regeneration process (Figure 8 (e)). Despite the magnitude difference, the growth trends of exergy efficiency concerning other objectives for both materials are the same. For instance, it increases with growing ICC (Figure 8 (a)) and m_{CO_2}(Figure 8 (c)) due to higher CO_2 concentration in the feed air and more CO_2 being successfully captured (more useful separation work). In contrast, it shows a mild decreasing trend with increasing δ_{save}. This is because increasing δ_{save} requires smaller mass flow rate of feed air $\dot{m}_f$, leading to less stale indoor air being treated per unit of time (Figure 8 (d)). Conversely, to attain more m_{CO_2}, the optimization inevitably sacrifices δ_{save} and thus presents a trade-off relationship in Figure 7 (i). As such, though sorbent MOF captures 46% more CO_2 per day, it achieves 53% lower δ_{save} than 13X (Figure 7 (f) and (g)). Another trade-off relationship can be observed in minimizing Z1 and maximizing Z3 (see Figure 7 (h)),

The short version of the paper was presented at ICAE2022, Bochum, Germany, Aug 8-11, 2022. This paper is a substantial extension of the short version of the conference paper.

imposed by the supply-demand balance of CO_2 mass. Specifically, maximizing Z3 requires higher Z1 as an ideal CO_2 supply, which is conflicting with the pursuit of good IAQ. Collectively, these conflicting objective pairs cannot achieve the desired values without sacrificing the other.

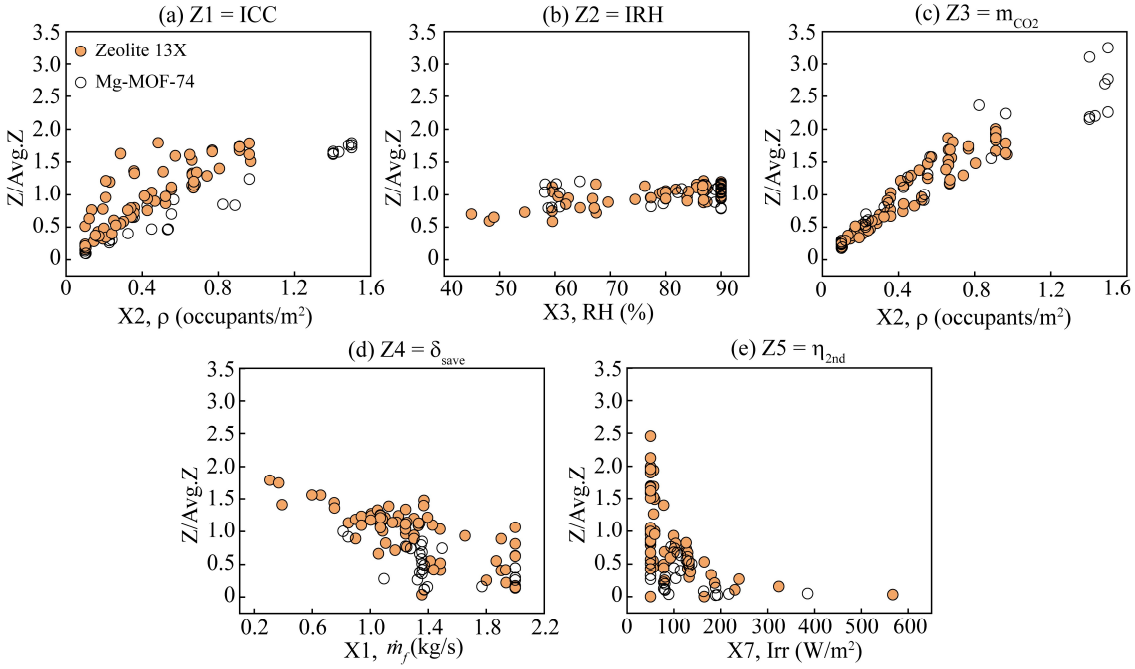

Figure 8. Effects of dominant parameters for 13X and MOF on different objectives: (a) influence of ρ on Z1; (b) influence of ambient RH on Z2; (c) influence of ρ on Z3; (d) influence of $\dot{m}_f$ on Z4; (e) influence of hourly mean *Irr* on Z5.

Figure 8 comparatively analyses the effects of different dominant parameters on objectives between the two adsorbents. For example, due to the higher CO_2 capacity [45], MOF can still maintain the ICC below 100 Pa for scenarios with higher occupancy rates, such as bars and concerts with occupancy ρ higher than 1. IRH is dominantly decided by ambient RH and has a relatively small fluctuation, compared to other objectives, due to the IRH constraint applied during the optimization process. m_{CO_2} increases when there are more occupants inside the room, with MOF solutions are mostly larger than 13X solutions. However, MOF shows lower enhancement in δ_{save} and η_{2nd} owing to its higher specific energy consumption than 13X,

4.2 Constrained optimization between Z1 and Z3

After locating that minimizing Z1 is conflicted with maximizing Z3, this section conducted a dual-objective optimization between them, with constraints applied. Here the material type is not treated as the 8th parameter but as two separate cases because of the overwhelming advantages of MOF on minimizing Z1 and maximizing Z3 than 13X. Figure 9 compares the Pareto front solutions with the first-iteration solutions to compare the optimization performances between two adsorbents. All the best trade-offs between minimizing Z1 and maximizing Z3 are observed in the Pareto front solutions (marked by pink starts in Figure 9 (a)). In contrast, Z1values of some of the first iteration solutions exceed 100 Pa, beyond which the design could not achieve plausible IAQ.

The short version of the paper was presented at ICAE2022, Bochum, Germany, Aug 8-11, 2022. This paper is a substantial extension of the short version of the conference paper.

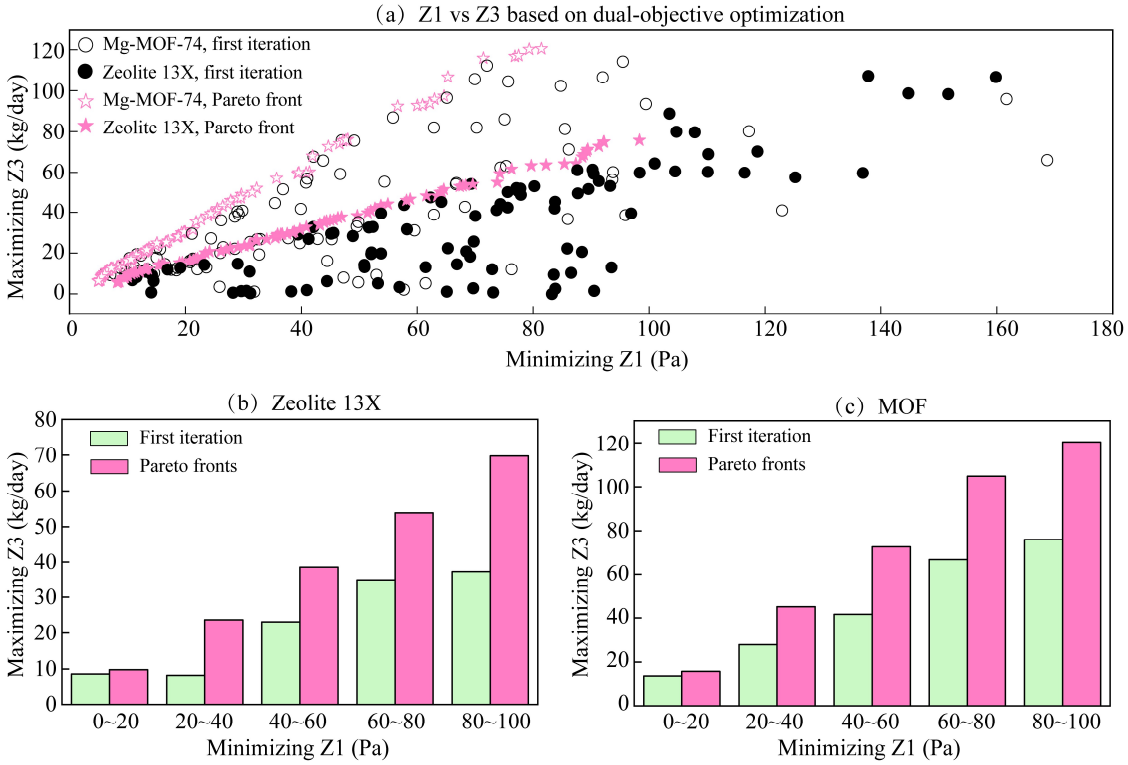

Figure 9. Dual-objective optimization between minimizing Z1 and maximizing Z3; (a) First iteration versus Pareto fronts; (b)-(c) Segmented comparisons.

Table 5. Compare the solutions numbers in different Z1 bounds between the first iteration and PF solutions.

Z1 (Pa)		0-20	20-40	40-60	60-80	80-100	>100
13X	Before	10	9	20	25	21	15
	After	29	29	18	13	11	0
MOF	Before	22	29	19	15	10	5
	After	61	19	9	10	1	0

Regarding the optimized Z3 values, MOF solutions demonstrate overwhelming advantages over 13X, as they capture an average of 27% more CO_2. Figure 9 (b) and (c) also depict the segmented optimization effects for 13X and MOF. Specifically, Z1 values are divided into five segments, with 20 Pa each. It can be observed that while maintaining the same Z1 range, the obtained Pareto fronts of both adsorbents can always remove more m_{CO_2} than the first-iteration solutions, indicating 74% and 59% enhancement for MOF and 13X, respectively. According to Table 5, the dual-objective optimization decreases the solution numbers for higher tiers of Z1 values and eliminates the solutions with Z1 higher than 100 Pa, achieving the objective of minimizing Z1.

Figure 10 shows the variation of Z1 and Z3 with respect to the crowdedness level, which is indicated by the ratio of ρ over the median ρ value of all the solutions. As ρ increases in Figure 10 (a), -Z1 decreases, indicating that the indoor CO_2 concentration increases due to more respiratory CO_2 being generated, enabling more CO_2 to be captured in Figure 10 (b). Z1 and Z3 values response oppositely towards ρ, which explains the existence of the trade-off between Z1 and Z3 (as shown in Figure 9 (a)).

The short version of the paper was presented at ICAE2022, Bochum, Germany, Aug 8-11, 2022. This paper is a substantial extension of the short version of the conference paper.

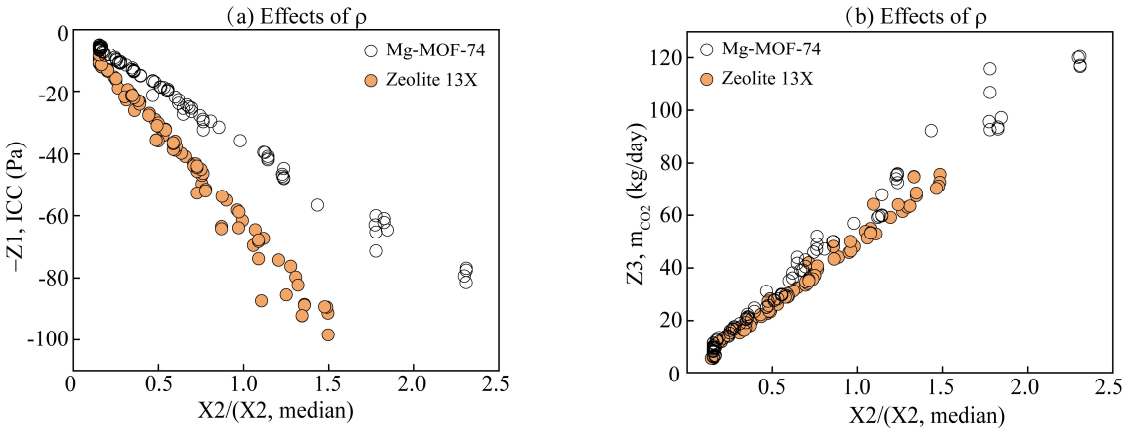

Figure 10. Effects of occupancy ρ on Z1 and Z3.

4.3 Constrained optimization between Z3 and Z4

This section conducted a dual-objective optimization between maximizing Z3 and Z4. Similar to the last section, this optimization has also applied constraints to the other 3 objectives to avoid impractical solutions and to ensure that all the comparisons are made on an even playing field. However, instead of separately investigating the two sorbent materials, this section considered the sorbent material type as the 8th parameter because they present dominant advantages in maximizing Z3 or Z4, respectively. In other words, it would be a good chance to put MOF and 13X in the same pool and allow them to exert pressure on each other to survive to the final iteration, by which system design quality can be further improved. As shown in Figure 11 (a), the 13X solutions exhibit 55% worse performance in maximizing Z3 due to lower CO_2 capacity and 82% higher in maximizing Z4 due to a lower specific energy consumption rate. Additionally, a major portion of first-iteration solutions fail to save AC energy consumption as compared with traditional cases, thus yielding negative δ_{save} (CO_2 regeneration energy consumption is included). This might be infeasible for energy-saving applications, but still, it is a feasible CO_2 capture device.

To evaluate the optimality of obtained solutions, a new parameter defined by the relative distance between a solution to the absolute optimal solution point, is introduced. According to Eq. (37), the position of any given solution is denoted as $(Z4(n), Z3(n))$ and that of the absolute optimal solution $(Z4(0), Z3(0))$ is equal to (1, 1) in a normalized coordinate axis. The closer to the point (1,1), the more optimized the solution is. As shown in Figure 11 (b), the relative distance of all the Pareto front solutions is shorter than that of the first iteration solutions. Figure 11 (c) presents the variation of average Z3 values for those solutions in the same δ_{save} segment. It is observed that while maintaining the same δ_{save} range, the Pareto front solutions can always achieve higher m_{CO_2} with an average enhancement of around six-fold. On the other hand, according to Table 6, the dual-objective optimization also eliminates the solutions with negative Z4 values and increases the solution numbers for higher tiers of Z4 values, as one of the objectives is to maximize Z4.

Table 6. Compare the solutions numbers in different Z4 bounds between the first iteration and PF solutions.

Z4 (%)	0-20	20-40	40-60	60-80	80-100	< 0
Before	7	13	3	6	1	70
After	6	13	31	44	6	0

The short version of the paper was presented at ICAE2022, Bochum, Germany, Aug 8-11, 2022. This paper is a substantial extension of the short version of the conference paper.

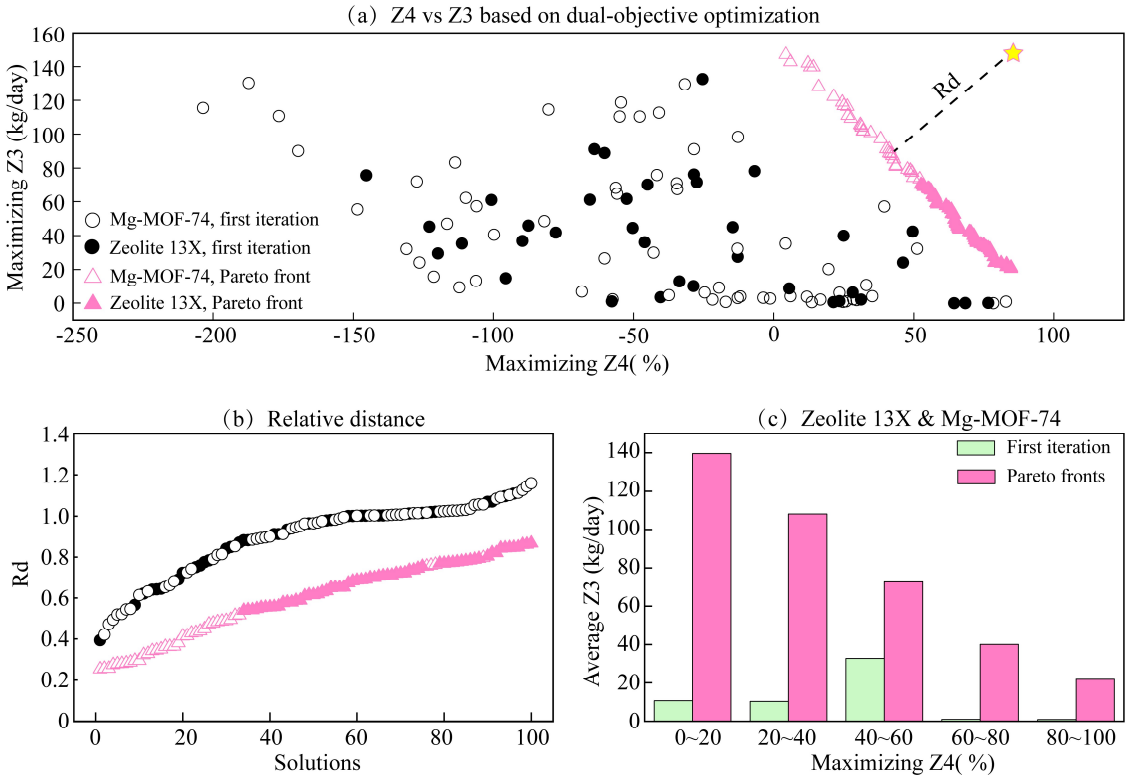

Figure 11. Dual-objective optimization of the solar-driven IC-VAC system: (a) maximizing Z4 and maximizing Z3; (b) Relative distance of first iteration and the Pareto fronts; (c) 13X and MOF's results from the first iteration and the Pareto fronts.

$$\mathrm{Rd} = \sqrt{(Z4(n) - Z4(0))^2 + (Z3(n) - Z3(0))^2} \tag{37}$$

To explain the conflicts between Z3 and Z4, Figure 12 presents their respective variations with respect to the three most significant parameters during the dual-objective optimization. For straightforward comparison, these parameters have been normalized. As $\dot{m}_f$ increases, Z3 increases while Z4 decreases, exhibiting opposite trends and resulting in their trade-off relationship (Figure 12 (a)). This is because, increasing $\dot{m}_f$ inevitably increases the fresh air exchange rate with the ambient during weak adsorption period, as well as increasing the thermal energy to desorb more captured CO_2. It can also be noticed that MOF solutions can handle a much higher $\dot{m}_f$ owing to their higher CO_2 capture capacity than 13X. Similar to $\dot{m}_f$, ρ has a positive relationship with Z3 while a negative one with Z4 (Figure 12 (b)). According to Figure 12 (c), the effects of m_a on 13X solutions is more obvious. Higher m_a captures more CO_2 but also consumes more regeneration heat, thus decreases the energy-saving potential. Interestingly, the sorbent mass has limited effects on MOF's Z3 and Z4 objectives, as shown in Figure 12 (c1) and (c2). A possible reason is that due to MOF's higher CO_2 capacity, the adsorbent mass at the given lower band already satisfies all the given constraints and occupancy scenarios. Thus, the optimization framework prioritizes MOF solutions with lower adsorbent mass to avoid large regeneration heat consumption and satisfy the exergy efficiency constraint. Considering that the market price of MOF is substantially higher than 13X, this framework also, to some extent, secures the economic feasibility of the IC-VAC system.

The short version of the paper was presented at ICAE2022, Bochum, Germany, Aug 8-11, 2022. This paper is a substantial extension of the short version of the conference paper.

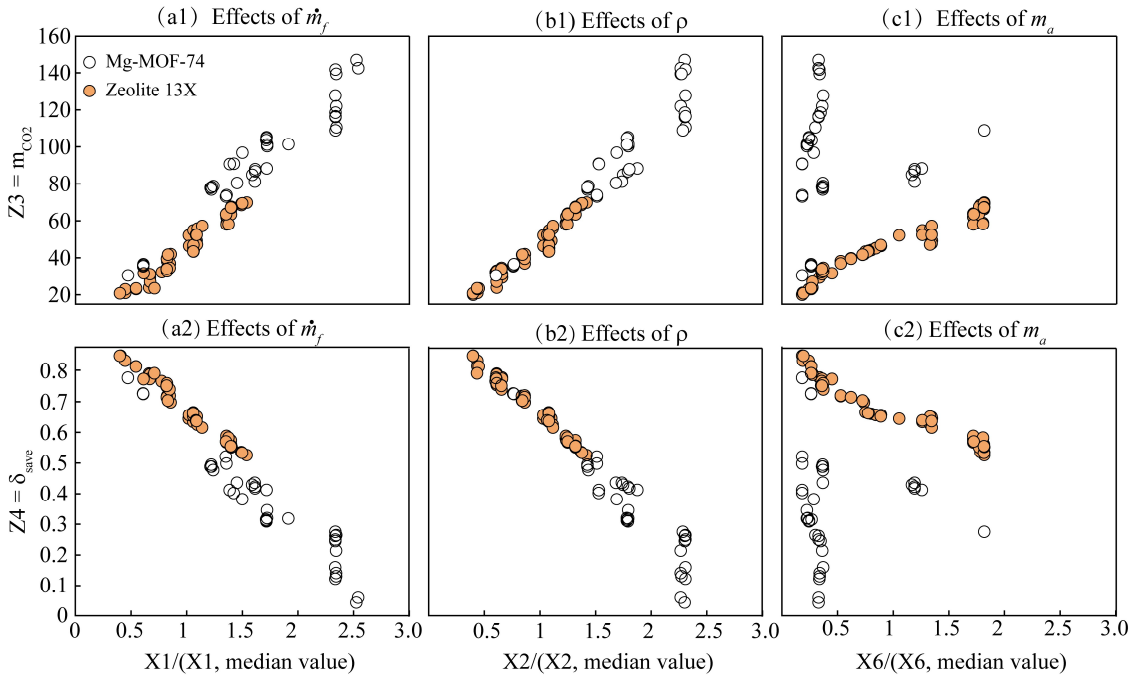

Figure 12. (a) – (c): Effects of X1, X2, X6 on the trade-off between Z3 and Z4 for both adsorbents.

4.4 Discussion

Stability and cyclability. To better understand the underlying reasons for 13X and MOF's different optimization behaviour, this section has compared the structure variation of these two sorbents after multiple adsorption-desorption cycles.

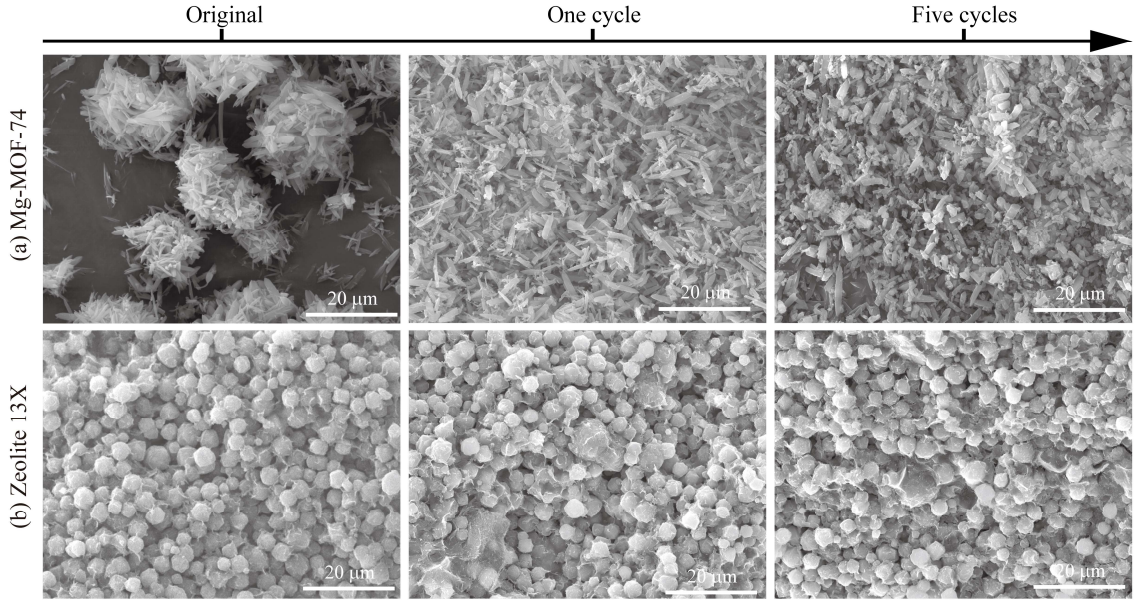

Figure 13. SEM images of MOF and Zeolites with comparisons among 0 cycles, 1 cycle and five cycles. (a) Mg-MOF-74; (b) Zeolite-13X.

During the sample-making procedure, a gas stream with above-ambient CO_2/H_2O concentration is driven through the two adsorbent samples (adsorption). Then, the test tubes were put into hot water with a constant temperature of 95 °C (regeneration). After being heated

The short version of the paper was presented at ICAE2022, Bochum, Germany, Aug 8-11, 2022. This paper is a substantial extension of the short version of the conference paper.

for 10 minutes, the samples were put into the refrigerator at a temperature of 4~5 ℃. Another group of 13X and MOF repeats the cooling-adsorption-heating-desorption process for five cycles. Then the original, one-cycle, and five-cycle samples are observed under TESCAN VEGA3 in Hong Kong, The Hong Kong Polytechnic University, for obtaining scanning electron microscopy imaging (SEM). The comparisons are shown in Figure 13. MOF shows higher sensitivity towards moisture, as its structures were vastly ruined. In contrast, 13X appears less sensitive to moisture and shows higher stability in cyclic use [22].

Economic feasibility. A 25-year cost analysis is conducted on 20 optimized solutions from 13X and MOF, respectively, based on Eq. (38). In this equation, the specific cost of CO_2 avoidance (SCC, USD/ton) is introduced and defined by the ratio of total cost over total captured CO_2 mass. The total cost mainly consists of 3 sectors: C_i is the investment capital cost in year "0", including the purchase of solar thermal collectors, adsorption columns, and other auxiliary systems; C_o is the operation cost, mainly including the electricity consumption by auxiliary devices, such as vacuum pumps, air blowers, etc.; a is the yearly inflation rate of 5%; C_m is the maintenance cost, mainly including the adsorbent replacement, e.g., once a year for 13X and twice a year for MOF. The price of 13X is 1.65 USD/kg referenced from Alibaba [48], and of MOF is 10 USD/kg predicted by [49, 50]. Among the costs, consumed adsorbent cost accounts for the dominant part [21], which is 61.13% and 81.9% for 13X and MOF, respectively (Figure 14). The total captured CO_2 mass is an accumulation over the 25-year lifespan [51]. The SCC for 13X fluctuates between 196 and 235 USD/ton, with a median value of 211.1 USD/ton, comparable to the other reported indoor capture costs (203.7 USD/ton [18] and 183.8 USD/ton [17]). These costs fall in the middle level of current low-concentration capture results (90 ~ 383 USD/ton, comparison details can be found in [17]). The SCC for MOF solutions is higher than that for 13X, with a range from 350 to 479 USD/ton and a median value of 395 USD/ton.

$$\mathrm{SCC} = \frac{(C_i + \sum_{j=0}^{25}(C_o^0 + C_m^0) \times (1+a)^j)}{\sum_{j=0}^{25} m_{CO_2,year}^j} \tag{38}$$

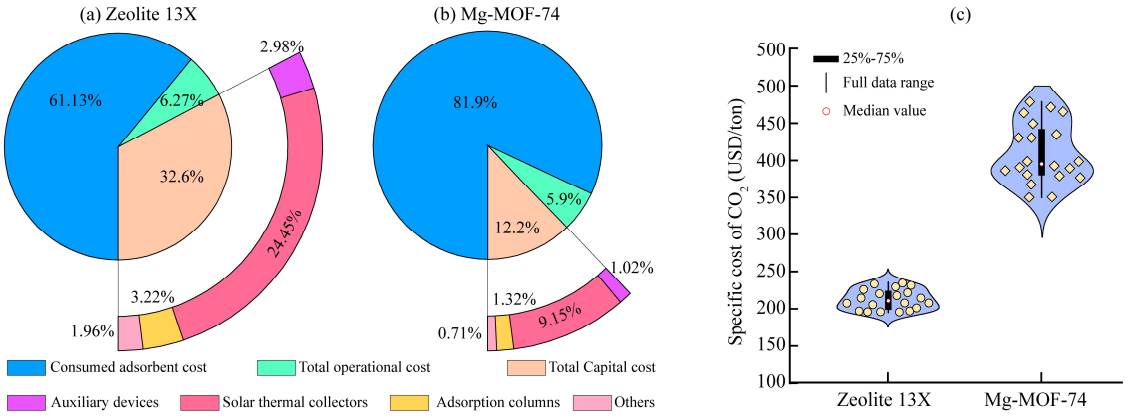

Figure 14. Detailed 25-year lifespan cost analysis results based on 20 Pareto front solutions from 13X and MOF, respectively. (a) ~ (b) The average cost sectors; (c) The specific cost for the two materials. In each violin plot, the box indicates the 25th–75th percentiles, the center line indicates the full data range and the white dot indicates the median value.

Literature comparison. The results of ICC control and the energy-saving potential of this study are compared with other references which adopted CO_2 capture as the stale indoor air treatment method. According to Figure 15 (a), while all the optimized solutions (including MOF and 13X solutions) can achieve ICC lower than 100 Pa, a large amount of the solutions can obtain even lower ICC values, i.e., < 50 Pa. This indicates our advantage in controlling indoor CO_2 concentration. Considering the better energy-saving potential of 13X solutions than

The short version of the paper was presented at ICAE2022, Bochum, Germany, Aug 8-11, 2022. This paper is a substantial extension of the short version of the conference paper.

MOF solutions, Figure 15 (b) compares 13X solutions with other publications regarding energy-saving. It can be seen that the optimized 13X solutions can achieve energy-saving potentials of higher than 50%, which outcompetes the other reported results.

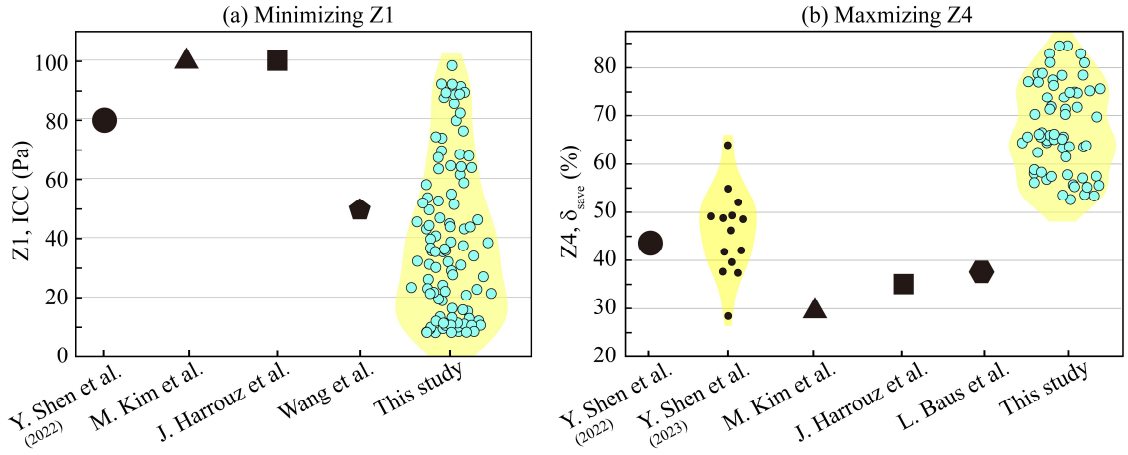

Figure 15. Compare the performances of optimized 13X solutions with different literature: (a) Comparison of minimizing Z1, the lower the better; (b) Comparison of maximizing Z4, the higher the better. Y. Shen et al. 2022 [17], Shen et al. 2023 [18], M. Kim et al. [14], J. Harrouz et al. [15], L. Baus et al. [16], Wang et al. [52].

5. Conclusion

While the solar-driven IC-VAC system holds the potential to simultaneously realize green building's merits, including high indoor air quality, low CO_2 emission, and low energy consumption, its applications are hampered by an ambiguous interplay between objectives that might be conflicting. This study has conducted an NSGA-II-based multi-objective optimization analysis of a dynamic solar-driven IC-VAC model to elucidate the relationship between conflicting objectives. This optimization framework has revealed the influences of dominant decision parameters and effectively improved the techno-energetic performances of the system compared to unoptimized solutions. This study premised its optimization and comparison on the strict obedience to given constraints to ensure a fair and practical analysis.

On the one hand, maximizing the CO_2 capture amount conflicts with minimizing indoor CO_2 concentration, which is mainly affected by indoor occupancy. Specifically, a higher occupancy results in more respiratory CO_2 being captured but poses a challenge in bringing indoor CO_2 concentration (ICC) to a healthy level. While maintaining the same level of ICC, the optimized solutions can capture more CO_2, with an improvement of 59% and 74% for 13X and MOF, respectively.

On the other hand, maximizing the CO_2 capture amount conflicts with maximizing energy-saving potential, which is collectively decided by three parameters, including the mass flow rate of feed air, occupancy, and adsorbent mass. Specifically, if ramped up, these parameters can increase the CO_2 removal amount but inevitably reduce the energy-saving potential due to increased CO_2 regeneration heat consumption and AC energy consumption. While achieving the same energy-saving potential level, the optimized solutions, including both adsorbent materials, capture an average of 6 times more CO_2 than the unoptimized solutions. Compared to MOF solutions, 13X solutions capture 55% less CO_2, but save 87% more energy owing to lower specific energy consumption and higher cyclability/stability shown in SEM images, demonstrating higher feasibility in indoor applications. Exemplified by an 80 m^2-sized room, this system could save up to 85% AC energy consumption with occupancy ranging from 0.26 to 0.9 occupants/m^2 while maintaining the indoor CO_2 concentration below 100 Pa.

The short version of the paper was presented at ICAE2022, Bochum, Germany, Aug 8-11, 2022. This paper is a substantial extension of the short version of the conference paper.

When being applied in buildings or other indoor spaces, the proposed indoor CO_2/H_2O capture system might cause noise and space occupation issues. Addressing these issues demand continual efforts in minimizing system sizes and developing high-capacity sorbent materials. More efforts could be directed to investigating the techno-energetic feasibility of more mature adsorbent materials and capture methods, to pinpoint the most suitable solutions for achieving green buildings. Moreover, this proposed framework can be further perfected by incorporating cost and environmental impacts as optimization objectives, thereby propelling the development of CO_2 capture-based ventilation and air conditioning system and ultimately the realization of sustainability.

6. Acknowledgement

The authors would like to thank The Hong Kong Polytechnic University for financial support via the research project with Ref. No. H-ZJMR.

The short version of the paper was presented at ICAE2022, Bochum, Germany, Aug 8-11, 2022. This paper is a substantial extension of the short version of the conference paper.

7. References

1. McCollum, D.L., et al., *Energy investment needs for fulfilling the Paris Agreement and achieving the Sustainable Development Goals.* Nature Energy, 2018. **3**(7): p. 589-599.
2. Zuo, J. and Z.-Y. Zhao, *Green building research–current status and future agenda: A review.* Renewable and Sustainable Energy Reviews, 2014. **30**: p. 271-281.
3. Wang, W., et al., *Conversion and storage of solar energy for cooling.* Energy & Environmental Science, 2022. **15**(1): p. 136-145.
4. Jacobson, T.A., et al., *Direct human health risks of increased atmospheric carbon dioxide.* Nature Sustainability, 2019. **2**(8): p. 691-701.
5. Steven J. Emmerich, W.S.D., James W. Axley, *Natural ventilation review and plan for design and analysis tool*. 2001, National Institute of standards and technology.
6. Clay Nesler, K.P.L., Bertrand Lasternas. *How to build smart, zero carbon buildings - and why it matters*. 2021; Available from: https://www.weforum.org/agenda/2021/09/how-to-build-zero-carbon-buildings/.
7. Goeppert, A., et al., *Air as the renewable carbon source of the future: an overview of CO2 capture from the atmosphere.* Energy & Environmental Science, 2012. **5**(7).
8. Heo, S., et al., *Dry Capture of Low-level CO2 from Public Indoor Spaces using Chemically Modified Carbonaceous Adsorbents - A Review.* Asian Journal of Atmospheric Environment, 2021. **15**(1): p. 12-24.
9. Park, J., et al., *Shaping of a Metal-Organic Framework-Polymer Composite and Its CO2 Adsorption Performances from Humid Indoor Air.* ACS Appl Mater Interfaces, 2021. **13**(21): p. 25421-25427.
10. Lee, J.W., et al., *Liquid-like adsorbent assembled by CNTs: Serving as renewable CO2 capture materials for indoor air.* Journal of Energy Chemistry, 2021. **63**: p. 574-584.
11. Kim, M., et al., *CO2 adsorption on zeolite 13X modified with hydrophobic octadecyltrimethoxysilane for indoor application.* Journal of Cleaner Production, 2022. **337**.
12. Kim, S., et al., *Nano-encapsulated solvent via pickering emulsion in NaOH aqueous solution for indoor CO2 capture.* Journal of CO2 Utilization, 2021. **51**.
13. Seok Chae, Y., et al., *Moisture-tolerant diamine-appended metal–organic framework composites for effective indoor CO2 capture through facile spray coating.* Chemical Engineering Journal, 2021.
14. Kim, M.K., et al., *A novel ventilation strategy with CO2 capture device and energy saving in buildings.* Energy and Buildings, 2015. **87**: p. 134-141.
15. Harrouz, J.P., et al., *Feasibility of MOF-based carbon capture from indoor spaces as air revitalization system.* Energy and Buildings, 2022. **255**.
16. Baus, L. and S. Nehr, *Potentials and limitations of direct air capturing in the built environment.* Building and Environment, 2022. **208**.
17. Shen, Y. and H. Yang, *Achieving reduced emission and enhanced air quality by designing a solar-driven indoor CO2 capture system.* Journal of Cleaner Production, 2022. **379**.
18. Shen, Y. and H. Yang, *Global performance analysis of a solar-driven indoor CO2/H2O capture system for air quality enhancement and cooling energy saving.* Energy Conversion and Management, 2023. **280**.
19. Ben-Mansour, R., N.A.A. Qasem, and M.A. Antar, *Carbon dioxide adsorption separation from dry and humid CO2/N2 mixture.* Computers & Chemical Engineering, 2018. **117**: p. 221-235.
20. Rogerson, L. *Humidity & Latent load's impact on cooling system design*. 2020; Available from: https://www.superradiatorcoils.com/blog/what-is-the-latent-load-in-a-cooling-system-and-why-does-it-matter.

The short version of the paper was presented at ICAE2022, Bochum, Germany, Aug 8-11, 2022. This paper is a substantial extension of the short version of the conference paper.

21. Raganati, F., F. Miccio, and P. Ammendola, *Adsorption of Carbon Dioxide for Post-combustion Capture: A Review.* Energy & Fuels, 2021. **35**(16): p. 12845-12868.
22. Fu, D., Y. Park, and M.E. Davis, *Confinement effects facilitate low-concentration carbon dioxide capture with zeolites.* Proc Natl Acad Sci U S A, 2022. **119**(39): p. e2211544119.
23. Chen, C., D.-W. Park, and W.-S. Ahn, *CO2 capture using zeolite 13X prepared from bentonite.* Applied Surface Science, 2014. **292**: p. 63-67.
24. Adhikari, A.K. and K.-S. Lin, *Improving CO 2 adsorption capacities and CO 2 /N 2 separation efficiencies of MOF-74(Ni, Co) by doping palladium-containing activated carbon.* Chemical Engineering Journal, 2016. **284**: p. 1348-1360.
25. Zhao, R., et al., *Solar-assisted pressure-temperature swing adsorption for CO2 capture: Effect of adsorbent materials.* Solar Energy Materials and Solar Cells, 2018. **185**: p. 494-504.
26. Hesami, M., R. Naderi, and M. Tohidfar, *Modeling and Optimizing Medium Composition for Shoot Regeneration of Chrysanthemum via Radial Basis Function-Non-dominated Sorting Genetic Algorithm-II (RBF-NSGAII).* Sci Rep, 2019. **9**(1): p. 18237.
27. Pal, P., et al., *Genetic algorithm optimized node deployment in IEEE 802.15.4 potato and wheat crop monitoring infrastructure.* Sci Rep, 2021. **11**(1): p. 8231.
28. Wang, Z., et al., *A comparative study of multi-objective optimization with ANN-based VPSA model for CO2 capture from dry flue gas.* Journal of Environmental Chemical Engineering, 2022. **10**(3).
29. Hao, Z., et al., *Efficient hybrid multiobjective optimization of pressure swing adsorption.* Chemical Engineering Journal, 2021. **423**.
30. Zhang, F.-y., et al., *Thermo-economic optimization of biomass-fired organic Rankine cycles combined heat and power system coupled CO2 capture with a rated power of 30 kW.* Energy, 2022. **254**.
31. Hao, Z., M.H. Barecka, and A.A. Lapkin, *Accelerating net zero from the perspective of optimizing a carbon capture and utilization system.* Energy & Environmental Science, 2022. **15**(5): p. 2139-2153.
32. Radwan, A., et al., *Development of a new vacuum-based photovoltaic/thermal collector, and its thermal and exergy analyses.* Sustainable Energy & Fuels, 2020. **4**(12): p. 6251-6273.
33. Kalyanmoy Deb, A.P., Sameer Agarwal, T. Meyarivan, *A fast and elitist multiobjective genetic algorithm NSGA-II.* IEEE TRANSACTIONS ON EVOLUTIONARY COMPUTATION, 2002. **6**(2).
34. Sharifi, M.R., et al., *A new optimization algorithm to solve multi-objective problems.* Sci Rep, 2021. **11**(1): p. 20326.
35. Bell, I.H., et al., *Pure and Pseudo-pure Fluid Thermophysical Property Evaluation and the Open-Source Thermophysical Property Library CoolProp.* Ind Eng Chem Res, 2014. **53**(6): p. 2498-2508.
36. Dantas, T.L.P., et al., *Carbon dioxide–nitrogen separation through adsorption on activated carbon in a fixed bed.* Chemical Engineering Journal, 2011. **169**(1): p. 11-19.
37. Mason, J.A., et al., *Application of a High-Throughput Analyzer in Evaluating Solid Adsorbents for Post-Combustion Carbon Capture via Multicomponent Adsorption of CO2, N2, and H2O.* Journal of the American Chemical Society, 2015. **137**(14): p. 4787-4803.
38. Simone Cavenati, C.A.G., and Alı´rio E. Rodrigues, *Adsorption Equilibrium of Methane, Carbon Dioxide, and Nitrogen on Zeolite 13X at High Pressures.* Journal of Chemical and Engineering Data, 2004.
39. Qasem, N.A.A. and R. Ben-Mansour, *Adsorption breakthrough and cycling stability of carbon dioxide separation from CO2/N2/H2O mixture under ambient conditions using 13X and Mg-MOF-74.* Applied Energy, 2018. **230**: p. 1093-1107.

The short version of the paper was presented at ICAE2022, Bochum, Germany, Aug 8-11, 2022. This paper is a substantial extension of the short version of the conference paper.

40. Haar, L., J.S. Gallagher, and G.S. Kell, *NBS/NRC Wasserdampftafeln: thermodynamische und Transportgrössen mit Computerprogrammen für Dampf und Wasser in SI-Einheiten*. 2013: Springer-Verlag.
41. 16798-1, E., *Energy performacne of buildings*, in *Ventilation for buildings*. 2019.
42. Alados-Arboledas, L., J. Vida, and F.J. Olmo, *The estimation of thermal atmospheric radiation under cloudy conditions.* International Journal of Climatology, 1995. **15**(1): p. 107-116.
43. Shen, Y., T. Hocksun Kwan, and H. Yang, *Parametric and global seasonal analysis of a hybrid PV/T-CCA system for combined CO2 capture and power generation.* Applied Energy, 2022. **311**.
44. Zhao, R., et al., *Carbon pump: Fundamental theory and applications.* Energy, 2017. **119**: p. 1131-1143.
45. Yang, D.-A., et al., *CO2capture and conversion using Mg-MOF-74 prepared by a sonochemical method.* Energy Environ. Sci., 2012. **5**(4): p. 6465-6473.
46. Jong-Seok Lee, J.-H.K., Jin-Tae Kim, Jeong-Kwon Suh, Jung-Min Lee, Chang-Ha Lee, *Adsorption Equilibria of CO2 on Zeolite 13X and Zeolite X Activated Carbon Composite.* Journal of Chemical and Engineering Data, 2002. **47**(5).
47. Kwan, T.H., X. Wu, and Q. Yao, *Thermoelectric device multi-objective optimization using a simultaneous TEG and TEC characterization.* Energy Conversion and Management, 2018. **168**: p. 85-97.
48. Alibaba. *Adsorbent zeolite 13x molecular sieve for CO2 removal*. 2023 [cited 2023 2nd May]; Available from: https://www.alibaba.com/product-detail/Adsorbent-Zeolite-13x-Molecular-Sieve-For_60701038274.html?spm=a2700.7724857.0.0.2b085faasjc2uT&s=p.
49. Peng, P., et al., *Cost and potential of metal–organic frameworks for hydrogen back-up power supply.* Nature Energy, 2022. **7**(5): p. 448-458.
50. DeSantis, D., et al., *Techno-economic Analysis of Metal–Organic Frameworks for Hydrogen and Natural Gas Storage.* Energy & Fuels, 2017. **31**(2): p. 2024-2032.
51. Zhao, R., et al., *Techno-economic analysis of carbon capture from a coal-fired power plant integrating solar-assisted pressure-temperature swing adsorption (PTSA).* Journal of Cleaner Production, 2019. **214**: p. 440-451.
52. Wang, W., et al., *Efficient removal of CO2 from indoor air using a polyethyleneimine-impregnated resin and its low-temperature regeneration.* Chemical Engineering Journal, 2020. **399**.

The short version of the paper was presented at ICAE2022, Bochum, Germany, Aug 8-11, 2022. This paper is a substantial extension of the short version of the conference paper.